

Experimental and numerical investigation of a bar-and-plate heat exchanger for enhanced latent thermal energy storage

Raza, Waseem; Tancon, Marco; Zanetti, Emanuele; Berto, Arianna; Rossi, Stefano; Azzolin, Marco

DOI

10.1016/j.est.2025.119064

Publication date

Document Version Final published version

Published in Journal of Energy Storage

Citation (APA)

Raza, W., Tancon, M., Zanetti, E., Berto, A., Rossi, S., & Azzolin, M. (2026). Experimental and numerical investigation of a bar-and-plate heat exchanger for enhanced latent thermal energy storage. *Journal of* Energy Storage, 141, Article 119064. https://doi.org/10.1016/j.est.2025.119064

Important note

To cite this publication, please use the final published version (if applicable). Please check the document version above.

Copyright

Other than for strictly personal use, it is not permitted to download, forward or distribute the text or part of it, without the consent of the author(s) and/or copyright holder(s), unless the work is under an open content license such as Creative Commons.

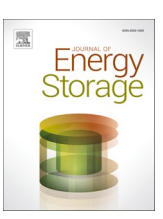
Please contact us and provide details if you believe this document breaches copyrights. We will remove access to the work immediately and investigate your claim.

ELSEVIER

Contents lists available at ScienceDirect

Journal of Energy Storage

journal homepage: www.elsevier.com/locate/est



Research papers

Experimental and numerical investigation of a bar-and-plate heat exchanger for enhanced latent thermal energy storage

Waseem Raza ^a, Marco Tancon ^a, Emanuele Zanetti ^b, Arianna Berto ^{a,*}, Stefano Rossi ^c, Marco Azzolin ^a

- ^a Department of Industrial Engineering, University of Padova, Via Venezia 1, Padova, 35131, Italy
- b Department of Process and Energy, Delft University of Technology, Leeghwaterstraat 39, 2628 CB, Delft, the Netherlands
- ^c Construction Technologies Institute, National Research Council, Corso Stati Uniti 4, Padova, 35127, Italy

ARTICLE INFO

Keywords: Latent thermal energy storage Phase change material PCM Heat transfer Bar-and-plate heat exchanger

ABSTRACT

Latent thermal energy storage (LTES) employing phase change materials (PCMs) offers a promising solution for thermal management in various applications, compensating for the intermittent and unstable characteristics of several thermal energy sources, such as solar energy. However, the inherently low thermal conductivity of PCMs hinders their heat transfer efficiency, resulting in extended charging and discharging times. This limitation can be addressed either by enhancing the thermal conductivity of the PCM or by optimizing the storage system geometry. In this study, two LTES configurations, finned and finless units based on bar-and-plate technology, were tested under different conditions of mass flow rate (100, 150, 200 kg h⁻¹) and heat transfer fluid (HTF) inlet temperature (46, 49, 52 °C), corresponding to temperature difference ($\Delta T_{thermal}$) of 3, 6 and 9 °C. To the best of the authors' knowledge, the bar-and-plate technology has been only marginally addressed in the context of LTES systems, and no comprehensive experimental investigations are currently available in the literature. The PCM employed, a paraffin wax (RT42), has a melting temperature ra nge between 38.2 °C and 42.5 °C. Results demonstrated that the finned unit reduced the melting time by up to 84 % compared to the finless configuration. At $\Delta T_{thermal} = 9$ °C and a mass flow rate of 200 kg h⁻¹, the charging process was completed within 2 hours for the finned unit versus about 8 hours for the finless unit. Moreover, for the finned unit, increasing $\Delta T_{thermal}$ from 3 °C to 9 °C resulted in a 28-50 % decrease in melting time, while an increase in the mass flow rate from 100 to 200 $kg \ h^{-1}$ shortened melting time by about 35 %. As a further step, the experimental data were used to validate a resistance-capacitance numerical model of the LTES unit, providing a valuable tool for LTES optimization and design according to specific application requirements. Unlike other available calculation methods, the developed model accounts for the explicit incorporation of fin geometry and PCM material in equivalent conductivities (PCM-fin composite) to capture the directional heat transfer pathways. Moreover, a parametric study was carried out to analyze the effect of fin parameters on melting time and energy storage.

1. Introduction

Climate change poses a critical threat to global sustainability. In response, the United Nations introduced Sustainable Development Goal (SDG) 7 [1], which calls for urgent action to make energy more accessible, affordable, reliable, and sustainable for all. The report emphasizes the need to increase the use of renewable energy sources and improve energy efficiency. This objective is strongly reinforced by international efforts, most notably the Paris Climate Agreement [2], adopted in December 2015, which underscores a shared commitment by nearly

every country to cut greenhouse gas emissions and phase out fossil fuel dependence. There has been a significant push to integrate renewable energy sources, such as solar and wind power, into the energy mix to address this challenge.

However, the intermittent nature of these renewables, exemplified by the variability of solar energy, presents challenges in maintaining a stable energy supply. Therefore, developing strategies to ensure a consistent and reliable energy system is fundamental. One promising solution to address the intermittency of renewable energy is thermal energy storage (TES). TES systems store excess thermal energy generated during periods of abundant renewable resource availability for

E-mail address: arianna.berto@unipd.it (A. Berto).

^{*} Corresponding author.

Nomenclature		t T	Fin thickness [m]	
A C PCM,s PCM,l CHTF Cal Dh DSC E Δh	Flow passage area [m²] Specific heat [J kg⁻¹ K⁻¹] Specific heat of PCM in solid phase [J kg⁻¹ K⁻¹] Specific heat of PCM in the liquid phase [J kg⁻¹ K⁻¹] Specific heat of heat transfer fluid [J kg⁻¹ K⁻¹] Specific heat of aluminum [J kg⁻¹ K⁻¹] Hydraulic diameter [m] Differential scanning calorimetry Energy [J] Latent heat of fusion [J kg⁻¹] Fin height [m]	T u V w_{th} $Greek\ l$ α Δ η λ $ ho$ σ	Temperature [°C, K] Standard uncertainty Volume [m³] Wall thickness [m] **Tetters** Heat transfer coefficient [W m² K²] Difference Charging cycle efficiency [¬] Thermal conductivity [W m² K²] Density [kg m³] Standard deviation	
HTF j k l L LTES m m n Np Nu PCM Pr Q R Re s	Heat transfer fluid Colburn factor [-] Coverage factor [-] Lance length of the fin [m] Width of water channel [m] Latent thermal energy storage Mass [kg] Mass flow rate of fluid [kg h ⁻¹] Number of fins per unit length [m ⁻¹] Number of measurements [-] Nusselt number [-] Phase change material Prandtl number [-] Heat flow rate [W] Thermal resistance [m ² K W ⁻¹] Reynolds number [-] Fin spacing [m]	τ μ Subscrip al amb app c ch e eff in melt out s up	Time [s] Viscosity [kg m ⁻¹ s ⁻¹] pts Aluminum Ambient Apparent Combined Channel Expanded Effective Inlet Melting Outlet Solidus Upper	

later use when energy demand is high or generation from renewable sources is low. This capability enhances system reliability and flexibility by storing surplus energy, facilitating the inclusion of renewable energy in the energy mix [3,4]. Primary TES methods include sensible, latent, and thermochemical, with latent thermal energy storage (LTES) using phase change materials (PCMs) that offer significant advantages.

PCMs are valued for their high energy density and ability to absorb and release large amounts of energy during phase change at nearly constant temperatures, making them highly effective for compact thermal energy storage. Compared to sensible heat storage, LTES offers a larger energy storage capacity [5]. The versatility of LTES is evident in its diverse applications, including solar heating [6], space heating [7], thermal management of electronic equipment [8,9], drying processes [10,11], waste heat recovery [12,13], and solar energy storage [14].

Despite their numerous advantages, PCMs are often limited by low thermal conductivity, which significantly impacts the heat transfer rate within PCM-based systems [15,16]. This leads to extended charging and discharging times, a challenge commonly referred to as the "rate problem." The rate problem hampers practical implementation and reduces the overall thermal performance of PCM-based thermal energy storage systems. Addressing the rate problem is essential to fully exploit the potential of PCMs for thermal energy storage. This necessitates developing strategies to minimize charging and discharging times while meeting specific application requirements.

Enhancing PCM thermal conductivity and optimizing the design of the LTES unit are critical strategies for improving the performance of LTES systems. The incorporation of metal foams [17,18], polyurethane foam [19], nanoparticles [20] as well as the adoption of encapsulated PCMs [21] and PCM composites [22], have shown promise in augmenting PCM thermal conductivity, but their impact on overall LTES performance has proved to be modest. Maxim and Dominic [23] demonstrated that even a fiftyfold increase in PCM thermal conductivity

resulted in only a maximum instantaneous power increase by a factor of 2 or 3, depending on the LTES configurations. In contrast, optimizing the heat exchanger geometry offers a more promising solution for enhancing LTES unit performance.

Numerous studies have explored innovative heat exchanger designs to overcome the challenges associated with the low thermal conductivity of PCM in LTES systems. Callaghan et al. [24] conducted an experimental investigation of a small-scale thermal energy storage system utilizing a coil-and-shell heat exchanger. The system, equipped with an aluminum coil, was tested using two PCMs (OM55 by PLUSS® and dodecanoic acid) to evaluate the heat transfer rates both for charging and discharging. Similarly, Ahmadi et al. [25] contributed to the field by studying a shell-and-tube heat storage unit with a spiral coil tube. Their numerical simulations demonstrated the significant impact of coil geometry on thermal performance, with a potential reduction in melting time up to 71.4 % when increasing the spiral coil diameter from 50 mm to 70 mm. Herbinger and Groulx [26] conducted an experimental parametric analysis on a finned tube-and-shell heat exchanger with a variable number of finned tubes. Their findings revealed that the temperature difference between the heat transfer fluid (HTF) and the PCM melting temperature is critical in determining the required heat transfer area, significantly influencing overall system efficiency. These results underscore the importance of precise temperature control and the employment of heat transfer enhancement methods, such as fins, for optimizing LTES performance.

One particularly effective geometric optimization technique involves the incorporation of conductive fins, which increase the surface area available for heat exchange, thereby significantly improving system performance. Torbarina et al. [27] developed a computational model of an LTES system utilizing a shell-and-tube configuration with longitudinal fins. Their numerical investigations revealed that increasing the HTF inlet temperature significantly enhances heat transfer between the HTF

and the PCM. A subsequent study by Shank et al. [28] investigated a shell-and-tube LTES system with various fin configurations attached to a central copper pipe. The researchers observed remarkable reductions in charging and discharging times, from 79 % to 50 %, when compared to a finless configuration, further emphasizing the pivotal role of fins in accelerating thermal processes within LTES systems. Fahad et al. [29] explored nine different fin configurations by combining two, three and four rectangular fins with straight, curved, and angled branching fins to improve the melting performance of PCM in shell and tube heat exchangers. Out of all the setups, the design with two rectangular fins with angled branching delivers the best results with a 85 % reduction in melting time and the highest energy storage rate.

In another study, Cao et al. [30] introduced an innovative method for storing energy by using river water flow to charge PCM-based thermal storage units. The findings showed that optimizing the unit's geometry and using thin, closely spaced fins resulted in a reduction of solidification time by up to 84.4 %. Lee et al. [31] focused on improving the melting performance of a cold thermal energy storage tank by incorporating stratified fins. Their novel design resulted in a 156 % increase in the average exchanged thermal power compared to a finless configuration. Safari et al. [32] examined PCM melting in rectangular tanks with rectangular, pin and perforated fins under various orientations. The rectangular fins reduced the melting time by 3.3 % and 8.3 % compared to perforated and pin fins, respectively. On the other hand, the perforated and pin fins required 71 % and 9 % less fin volume, respectively, than the rectangular fin configuration. Hamid and Mehrdoost [33] numerically explored performance enhancement of a shell-and-tube LTES unit using sinusoidal wavy fins and various tube shapes. Doublepitch sinusoidal fins reduced melting time by 9.5 % compared to straight fins. Increasing HTF tubes from one to four decreased melting time by 38.3 %. Petal-shaped tubes with nine petals further reduced charging time by 24 % compared to circular tubes and 57 % compared to the baseline case with one circular tube and straight fins.

Bar-and-plate technology offers a specific design of stacked bars and plates that create a network of channels for fluid flow [34]. This configuration optimizes heat transfer by maximizing fluid contact area while minimizing flow resistance. Renowned for their modularity and compactness, bar-and-plate heat exchangers represent a suitable solution for latent thermal energy storage, overcoming the challenges posed by the low thermal conductivity of phase change materials. Indeed, this technology facilitates improved heat transfer efficiency, reduced charging and discharging times, and contributes to more efficient and reliable thermal energy storage solutions that can better integrate renewable energy sources into the energy mix.

The literature shows that previous studies have investigated various LTES unit configurations (e.g., packed bad, shell and tube, flat plates), analyzing their performance under different operating conditions and fin geometries. However, to the best of authors' knowledge, the application of bar-and-plate technology to latent thermal energy storage has been only marginally addressed and no comprehensive investigation is currently available in the literature. The present work addresses this gap by experimentally investigating the performance of two LTES units (finned and finless) based on bar-and-plate technology using paraffin wax RT42 as PCM (melting temperature range between 38.2 $^{\circ}\text{C}$ and 42.5 $^{\circ}$ C). The dimensions of the units are 108 cm \times 17 cm \times 31.5 cm, with the finned device equipped with 1400 trapezoidal fins, each 0.03 cm thick and 1.2 cm wide, arranged in ten layers. Building on the well-established bar-and-plate heat exchanger concept, standardized by ALPEMA [35], the finned configuration offers structural robustness, scalability and industrial feasibility. Compared with common LTES geometries (e.g., shell-and-tube or flat-plate) and with available commercial units [36], the use of trapezoidal fins enhances heat transfer and accelerates phase change, while the flexibility in the fin geometry (thickness, height, pitch) allows the system to be tailored either for higher energy storage capacity or for rapid thermal response, depending on application needs.

The present investigation focuses on the PCM's transient

temperature, melting time, and heat transfer rate under varying secondary fluid inlet temperatures (46, 49 and 52 $^{\circ}\text{C}$) and flow rate conditions (100, 150 and 200 kg h $^{-1}$). As a further step, a resistance-capacitance numerical model of the LTES unit is developed. Unlike other available calculation methods, the developed model accounts for the explicit incorporation of fin geometry and PCM material in equivalent thermal conductivities (PCM-fin composite) to capture the directional heat transfer pathways. After validation against the present database, the model is employed to explore the effect of key design parameters (such as fin thickness, height and pitch) on the performance of the LTES unit. This model can serve as a tool for tailoring unit geometry according to the specific needs, whether prioritizing maximum energy storage or faster melting time.

2. Experimental methodology

2.1. Experimental setup

An experimental setup was developed to evaluate the heat transfer performance of finned and finless latent thermal energy storage units during the charging process. The platform, shown in Fig. 1a) and schematically in Fig. 1b), consisted of the following major components: a thermal energy storage unit, a water circulating bath (Thermo Scientific Haake G50 Ultra), a thermal flywheel equipped with a submerged electrical resistance heater, a Coriolis mass flow meter (Siemens SITRANSFC MASS 2100), two and three-way valves, T-type thermocouples (Tersid), an Ice Point Reference (KAYE K170) and a data acquisition module (Agilent 34970A).

The test section comprised a horizontally oriented aluminum LTES unit manufactured using bar-and-plate technology [35] (Fig. 2). For comparison, a finless unit with identical dimensions was also constructed. The finned LTES unit measures 108 cm \times 17 cm \times 31.5 cm, with a PCM cavity of 100 cm \times 12 cm \times 31 cm. The finned unit has a total mass of 46.7 kg, whereas the finless unit weighs 29.7 kg. Within the PCM cavity, 1400 trapezoidal fins (0.3 mm thick, 12 mm high, 8.3 mm pitch) were arranged in ten layers to provide a compromise between extended heat transfer area, structural stability and manufacturability. Compared to other fin types reported in the literature (e.g., wavy, perforated, serrated), these fins represent a practical and effective solution, offering competitive heat transfer performance while maintaining simplicity of fabrication, robustness and cost-effectiveness [32]. Distilled water was used as the heat transfer fluid, flowing through two flat channels (3 mm thick) located on either side of the PCM cavity. Offset strip fins (0.2 mm thick, 3 mm high, 3 mm pitch) were inserted into the water channels to promote earlier flow transition to turbulence and enhance convective heat transfer with an acceptable pressure drop. The entire test rig was insulated to minimize heat losses to the environment, and a 1 cm thick and 7 cm high Lexan glass sheet is mounted on the top of the aluminum frame to accommodate the volume expansion of the PCM during the charging process.

A total of 35 T-type thermocouples were used to monitor system temperatures at multiple positions. Among these, 32 thermocouples (numbered 1 to 32) were placed inside the PCM cavity, arranged in eight groups of four along two horizontal rows. These groups were spaced 20 cm apart in the horizontal direction within the cavity, with the spacing maintained by a plastic strip. One row was positioned at the cavity centre, while the other was located near the HTF channel. Each group spanned four vertical depths: the first probe was placed 6 cm below the PCM top layer, while the fourth probe was positioned 24 cm below the top (i.e., 7 cm above the cavity bottom). The detailed arrangement of PCM temperatures is shown in Fig. 3. In addition to PCM temperature measurements, two thermocouples are positioned at the inlet and outlet of the water channel to measure the water temperatures and one thermocouple is used to monitor the ambient temperature. To facilitate spatial analysis, the unit was divided into four horizontal zones, with Zone 1 near the HTF inlet and Zone 4 close to the HTF outlet. Before

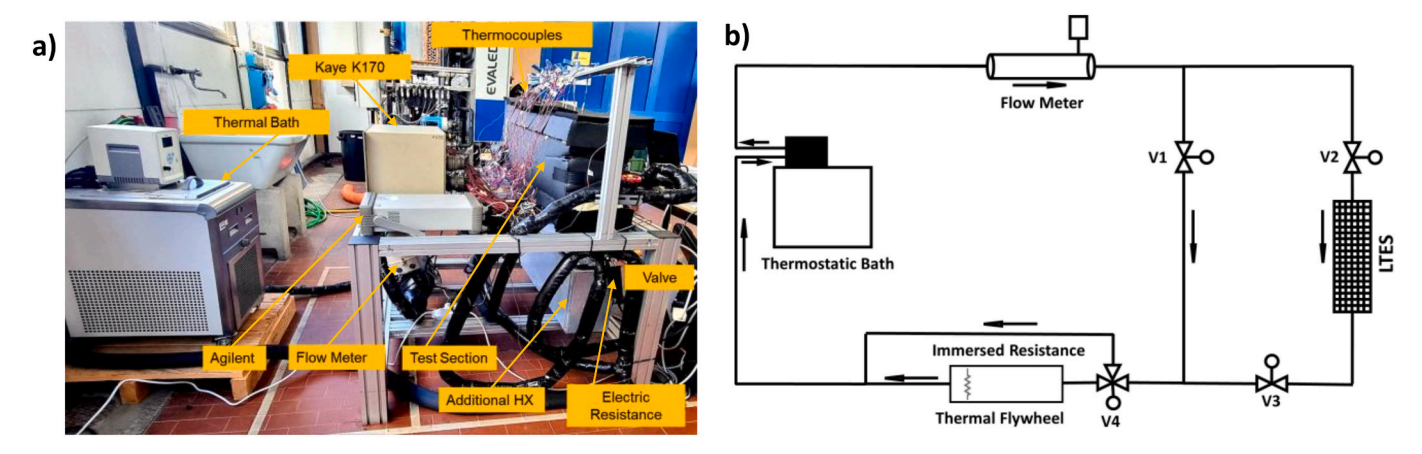


Fig. 1. a) Picture of the experimental setup with the positions of the main components highlighted. b) Schematic of the heat transfer fluid loop connected to the LTES unit.

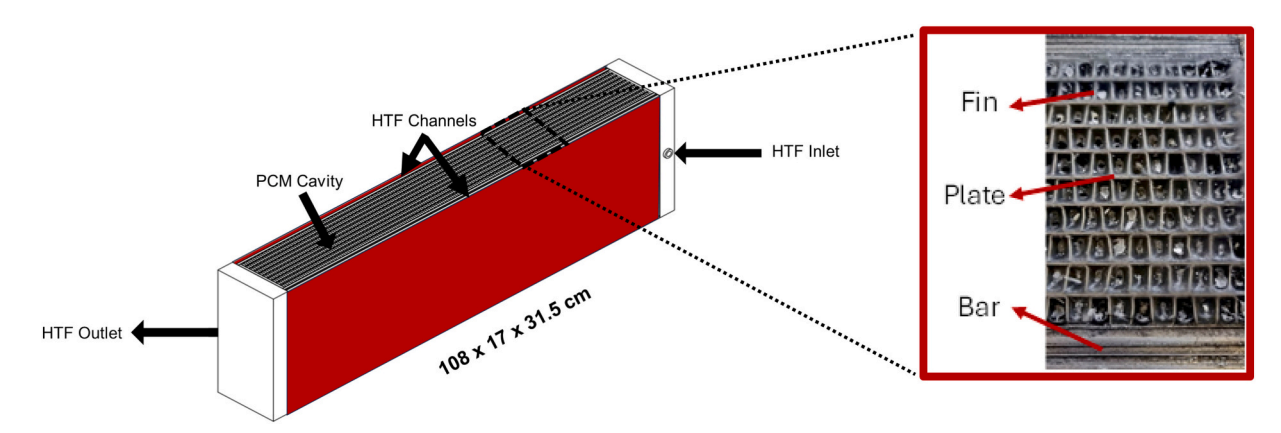


Fig. 2. LTES test section fabricated through bar-and-plate technology with conductive fins: 3D model of the unit and picture of the top view.

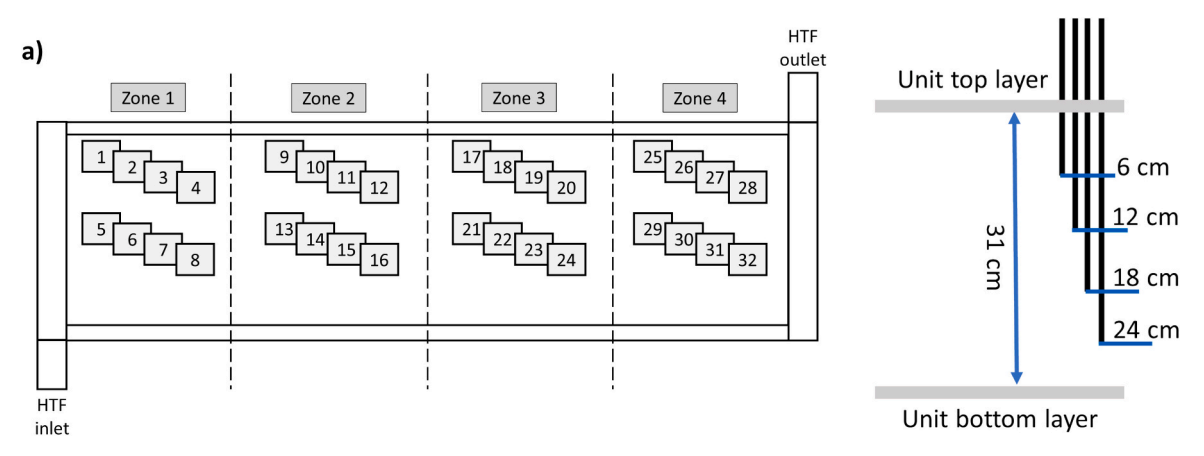


Fig. 3. a) Schematic of the thermocouples' position in the PCM cavity. b) Details of a set of four thermocouples placed at different depths inside the PCM.

testing, all thermocouples were calibrated using a FLUKE 1586A SUPERDAQ over the operating temperature range of 20–65 $^{\circ}\text{C}.$ The calibration yielded a measurement uncertainty of ±0.1 K.

The heat transfer fluid loop was designed to maintain a constant inlet temperature at the LTES unit throughout testing. Flow rate control was achieved using a combination of two-way valves (V1, V2, V3) and a three-way valve (V4), which allowed precise adjustment of the circulating flow. A Coriolis mass flow meter (accuracy ± 0.1 % of the measured value) ensured accurate flow rate measurements. The HTF was circulated by a thermal bath equipped with a PID controller to

regulate the inlet temperature.

As depicted in Fig. 1b), a thermal flywheel equipped with a submerged $2\,\mathrm{kW}$ electrical resistance heater was incorporated into the loop. The flywheel increased the overall thermal capacity of the system, compensating for the high initial heat transfer rate between the HTF and PCM, which temporarily exceeded the thermal bath's $2\,\mathrm{kW}$ heating capacity. This addition ensured a stable inlet temperature during the charging process.

The LTES unit was filled with 26.6 kg of PCM RT42, a commercialgrade phase change material manufactured by Rubitherm GmbH. The thermophysical properties of RT42 were initially referenced from the manufacturer's datasheet. However, since RT42 is a commercial PCM rather than pure paraffin, its properties were independently verified through experimental measurements using Differential Scanning Calorimetry (DSC). The DSC analysis provided detailed thermal properties of RT42, as illustrated in the heat flow rate per unit of mass versus temperature plot in Fig. 4. The primary measurement of DCS is heat flow rate, which represents the rate at which the sample absorbs or releases heat during the analysis. The DSC experiments revealed that the specific heat capacity of RT42 in its solid phase varied with temperature. It increased linearly from 2200 J kg $^{-1}$ K $^{-1}$ at 10 °C to 3104 J kg $^{-1}$ K $^{-1}$ at 37 °C. In its liquid phase, the specific heat capacity was 2360 J kg $^{-1}$ K $^{-1}$. The average onset temperature for melting was determined to be 38.2 °C, and the heat of fusion was found to be 148 kJ kg $^{-1}$. A summary of the physical properties of RT42 is presented in Table 1.

2.2. Experimental methodology

Prior to charging, the HTF was prevented from entering the unit until it reached the required inlet temperature. This was achieved by diverting the flow through a bypass line controlled by valve V1 (see Fig. 1b). A thermocouple continuously monitored the bypassed HTF temperature. Once the setpoint was reached, V1 was closed, and V2 and V3 were opened, directing the HTF into the LTES unit, starting the charging process.

Temperature data were acquired every 5 s using a data acquisition system (Agilent 34970A). The data is collected and analyzed using a computer running LabVIEW software. Each test was terminated when the HTF outlet temperature reached steady state, defined as the condition where the time derivative of the HTF outlet temperature approached zero. This ensured that the system had reached quasi-steady thermal equilibrium and no further changes in the thermal response of the system were detected thereafter.

A series of experiments was conducted under different inlet HTF temperatures and flow rate conditions (see Table 2), enabling systematic evaluation of the thermal performance of both finned and finless LTES units.

Here, $\Delta T_{thermal}$ represents the difference between HTF inlet temperature and upper melting temperature of phase change material, as defined in Eq. (1).

$$\Delta T_{thermal} = T_{HTF_in} - T_{up_melt} \tag{1}$$

By measuring the HTF temperature difference across the LTES unit (ΔT_{HTF}) and the mass flow rate reading of the Coriolis flow meter (\dot{m}_{HTF}), the heat transfer rate from the HTF to the LTES unit can be calculated as follows:

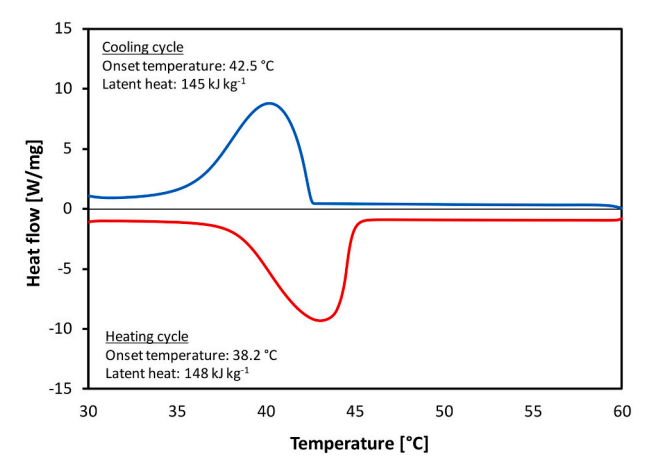


Fig. 4. DSC analysis of RT42 heat flow against temperature.

Table 1 Thermophysical properties of RT42.

Property	Value		
Density [kg m ⁻³]	880 (solid)		
	760 (liquid)		
Specific heat [J kg ⁻¹ K ⁻¹]	2200 at 10 °C (solid)		
	2360 (liquid)		
Thermal conductivity [W m ⁻¹ K ⁻¹]	0.26		
Viscosity [kg m ⁻¹ s ⁻¹]	0.02		
Latent heat [kJ kg ⁻¹]	145 (solid)		
	148 (liquid)		
Solidus temperature [°C]	38.2		
Liquidus temperature [°C]	42.5		

Table 2Operative conditions of experimental tests.

Test name	Flow rate [kg h ⁻¹]	$\Delta T_{thermal}$ [°C]	
3_100		3	
6_100	100	6	
9_100		9	
3_150		3	
6_150	150	6	
9_150		9	
3_200		3	
6_200	200	6	
9_200		9	

$$Q = \dot{m}_{HTF} \cdot c_{HTF} \cdot \Delta T_{HTF} \tag{2}$$

where Q is the heat flow rate and c_{HTF} is the specific heat of the water.

2.3. Heat loss correction and energy balance

Although the LTES unit was fully insulated, thermal losses towards the environment occurred in all experiments. To quantify these losses, a series of tests was carried out using water as the heat transfer fluid, with inlet temperatures varied between 16 $^{\circ}\text{C}$ and 65 $^{\circ}\text{C}$ while the PCM cavity was left empty. For each operating condition, inlet and outlet water temperatures, ambient air temperature and the HTF mass flow rate were recorded. The mean water temperature was calculated as:

$$T_{HTF_mean} = \frac{T_{HTF_in} + T_{HTF_out}}{2} \tag{3}$$

The temperature difference with the ambient was obtained as:

$$\Delta T_{amb} = T_{HTF_mean} - T_{amb} \tag{4}$$

At each time step, the heat loss rate to the environment was calculated as:

$$Q_{loss} = \dot{m}_{HTF} \cdot c_{HTF} \cdot \Delta T_{HTF,loss} \tag{5}$$

where $\Delta T_{HTF,loss}$ is the HTF temperature difference across the LTES unit measured during tests to evaluate thermal losses. To obtain a representative value, Q_{loss} was averaged over the entire test duration. For instance, at a water-to-ambient temperature difference of $\Delta T_{amb}=19.0$ K, the measured average heat loss was equal to 18.4 W.

After determining the rate of heat loss to the ambient environment, this value was subtracted from the measured heat transfer rate, which provided the actual heat transfer rate to the LTES. With the corrected heat transfer rate, the energy transferred by HTF is calculated using Eq. (6).

$$E_{HTF} = \int_{\tau_1}^{\tau_2} (\dot{m}_{HTF} \cdot c_{HTF} \cdot \Delta T_{HTF} - Q_{loss}) \cdot d\tau$$
 (6)

where E_{HTF} is the total energy released by HTF, Q_{loss} the heat flow rate from the LTES unit to the surroundings, and $\Delta \tau = \tau_1 - \tau_2$ is the test

duration. On the other hand, the energy stored in the PCM over a charging cycle was calculated by combining the energy absorbed by the PCM during sensible heating of solid, solid-liquid phase change and sensible heating of liquid, as follows:

$$E_{PCM} = m_{PCM} \cdot c_{PCM,s} \cdot \Delta T_s + m_{PCM} \cdot \Delta h + m_{PCM} \cdot c_{PCM,l} \cdot \Delta T_l$$
(7)

where E_{PCM} is the total energy stored in PCM, m_{PCM} is the mass of PCM in the LTES, $c_{PCM,s}$ is the specific heat of PCM in solid phase, $c_{PCM,l}$ is the specific heat of PCM in liquid phase, ΔT_s is the temperature difference between PCM's initial temperature and the lower melting temperature of PCM, ΔT_l is the temperature difference between the PCM upper melting temperature and the HTF inlet temperature, Δh is the latent heat of fusion required to melt the PCM (Table 1).

Additionally, Eq. (8) is used to calculate the energy absorbed by the aluminum (E_a) :

$$E_{al} = m_{al} \cdot c_{al} \cdot \Delta T_{al} \tag{8}$$

where m_{al} is the mass of aluminum, c_{al} is the specific heat capacity of aluminum, and ΔT_{al} is the temperature difference between the final and initial temperature of aluminum.

2.4. Uncertainty and repeatability analysis

The experimental uncertainty associated with the measured parameters was evaluated based on the procedure outlined in JCGM guidelines [37]. The total uncertainty consists of two components: Type-A and Type-B contributions. The Type-A uncertainty, which accounts for statistical variability in repeated measurements, is calculated using the equation:

$$u_A = \frac{\sigma}{\sqrt{N_p}} \tag{9}$$

where σ is the standard deviation of the measured data, and N_p is the total number of measurements.

Type-B uncertainty originates from calibration procedures and instruments' specifications and includes contributions from the Coriolis mass flow meter (± 0.1 % of the measured value) and thermocouples (± 0.1 K). The combined uncertainty is then determined as follows:

$$u_{c} = \sqrt{u_{A}^{2} + u_{B}^{2}} \tag{10}$$

For the heat flow rate, the combined standard uncertainty was calculated by applying the law of propagation of uncertainty as follows:

$$u_{Q} = \sqrt{\left(u_{c,m}\right)^{2} \cdot \left(\frac{\partial Q}{\partial m}\right)^{2} + \left(u_{c,T_{HTF,in}}\right)^{2} \cdot \left(\frac{\partial Q}{\partial T_{HTF,in}}\right)^{2} + \left(u_{c,T_{HTF,out}}\right)^{2} \cdot \left(\frac{\partial Q}{\partial T_{HTF,out}}\right)^{2}}$$
(11)

Finally, the expanded uncertainty was obtained by applying a coverage factor k = 2, which corresponds to a 95 % confidence level:

$$u_{Q,e} = u_Q \cdot k \tag{12}$$

The average combined uncertainty of the heat flow rate was approximately ± 3 %, while the average expanded uncertainty across the entire experimental dataset was ± 6 %.

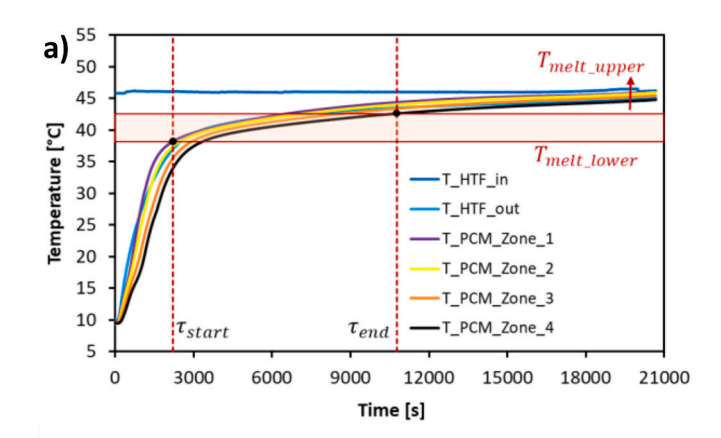
To assess the repeatability of the experiments, each test was repeated twice under identical operating conditions. The comparison showed good agreement: at $\Delta T_{thermal} = 9$ °C and $\dot{m}_{HTF} = 200$ kg h⁻¹, the PCM temperatures differed by less than 1 K throughout the experiment and, in terms of melting time, the standard deviation between repetitions was below 6 %, confirming the reliability of the experimental procedure.

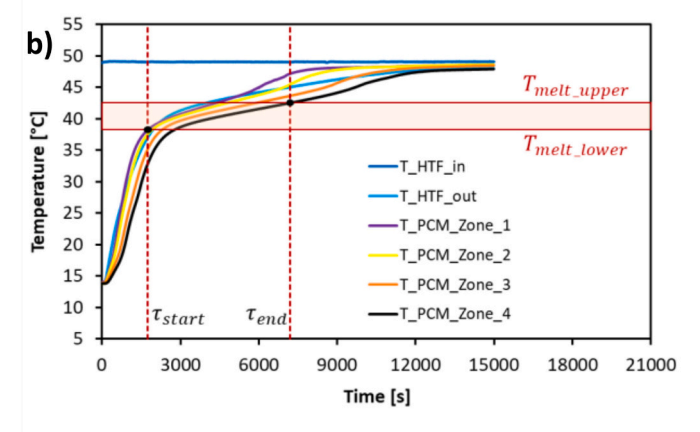
3. Experimental results

3.1. Finned LTES unit

Several experiments were conducted to evaluate the thermal performance of LTES design (finned and finless) with PCM during the charging process. The experiments began with the circulation of HTF through the channels until the PCM was fully charged. Key performance indicators such as melting time, thermal power, and energy stored in the PCM were analyzed under various conditions (see Table 2). Fig. 5 presents the average temperature profiles of the PCM over time for different zones within the LTES system. The tests were performed at a constant mass flow rate of 100 kg h $^{-1}$, with $\Delta T_{thermal}$ of 3 °C, 6 °C and 9 °C, corresponding to Fig. 5a), 5b), 5c), respectively. Each graph displays the average PCM temperature profiles in four distinct PCM zones as well as the inlet and outlet HTF temperatures.

As shown in Fig. 5a) ($\Delta T_{thermal} = 3$ °C), Zone 1 reaches the lower





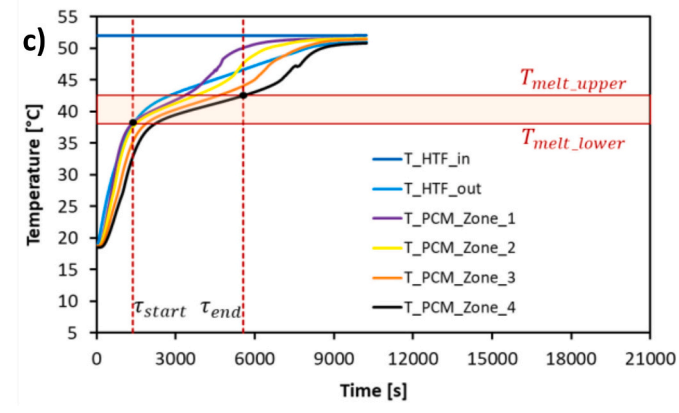


Fig. 5. PCM and HTF temperature profiles for the finned LTES unit at fixed mass flow rate (100 kg h $^{-1}$) and different $\Delta T_{thermal}$: a) 3 °C, b) 6 °C, c) 9 °C.

melting temperature (38.2 °C) at 2210 s and the upper melting temperature (42.5 °C) at 6445 s. In contrast, Zone 4, located farthest from the inlet, achieves these temperatures much later, at 3360 s and 10,495 s, respectively. This indicates that the heat transfer rate along the PCM cavity is not uniform. The delayed thermal response in Zone 4 can be primarily attributed to the reduction in the HTF temperature along the water channel as consequence of the heat rejected to the PCM in correspondence of the previous zones. In practical applications, such nonuniform temperature distribution in the HTF may cause localized thermal inefficiencies or incomplete energy utilization if the system is cycled prematurely. In Fig. 5b) ($\Delta T_{thermal} = 6$ °C), the increased thermal gradient results in a more rapid temperature rise. Zone 1 reaches the lower melting temperature earlier (~1745 s), with phase change completing at around 4360 s, while Zone 4 completes melting at ~7190 s. Compared to the $\Delta T_{thermal} = 3$ °C case, the higher $\Delta T_{thermal}$ results in a higher thermal power output during charging cycles and a more uniform latent heat absorption across the PCM volume. Fig. 5c), which refers to $\Delta T_{thermal} = 9$ °C, shows even more accelerated melting across all zones. The higher inlet temperature significantly increases the driving force for heat transfer, resulting in shorter melting times and improved charging performance. In particular, the temperature profiles show that Zone 1 completes melting at \sim 3315 s, while Zone 4 at \sim 5560 s.

The melting temperature range, highlighted by horizontal lines (38.2–42.5 °C), represents the phase change window of the PCM. Two vertical dashed lines indicate the beginning (τ_{start}) and end (τ_{end}) of the phase change process of melting, calculated using Eq. (13) as the period from when Zone 1 reaches the lower melting temperature to when Zone 4 reaches the upper melting temperature. This approach ensures that charging time reflects the performance of the entire LTES unit.

$$\tau_{melt,PCM} = \tau_{end} - \tau_{start} \tag{13}$$

As shown in Fig. 5, the temperature difference ($\Delta T_{thermal}$) strongly influences the charging dynamics. Specifically, larger thermal gradients enhance heat transfer rates, thereby promoting faster energy absorption and shorter charging times. At $\Delta T_{thermal}=3$ °C, the complete PCM charging process takes approximately 13540 s. Increasing the $\Delta T_{thermal}$ to 6 °C reduces the charging time by about 7 % (to 12635 s), while a further increase to $\Delta T_{thermal}$ to 9 °C shortens it by 28 % (to 9768 s).

Fig. 6 illustrates the trend of the melting time (as described by Eq. 13) versus the temperature difference ($\Delta T_{thermal}$ equal to 3, 6 and 9 °C) for mass flow rates equal to 100, 150, and 200 kg h⁻¹. The results clearly show that both the $\Delta T_{thermal}$ and mass flow rate are important parameters influencing the phase change dynamics of the PCM. As $\Delta T_{thermal}$ increases from 3 °C to 9 °C, the melting time significantly decreases across all tested mass flow rates. For instance, at a flow rate of 150 kg h⁻¹, when $\Delta T_{thermal}$ increased from 3 °C to 6 °C, the melting time decreased by approximately 39 %, from 6755 s to 4170 s. Further increasing $\Delta T_{thermal}$

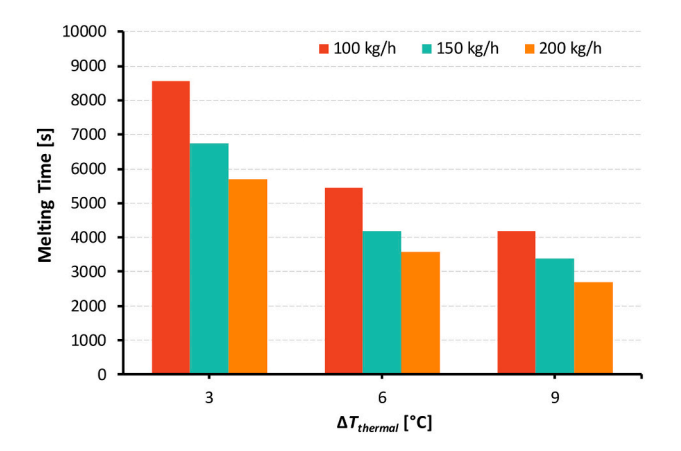


Fig. 6. Effect of HTF temperature difference ($\Delta T_{thermal} = 3$, 6, 9 °C) and mass flow rate (100, 150, 200 kg h⁻¹) on PCM melting time for the finned LTES unit.

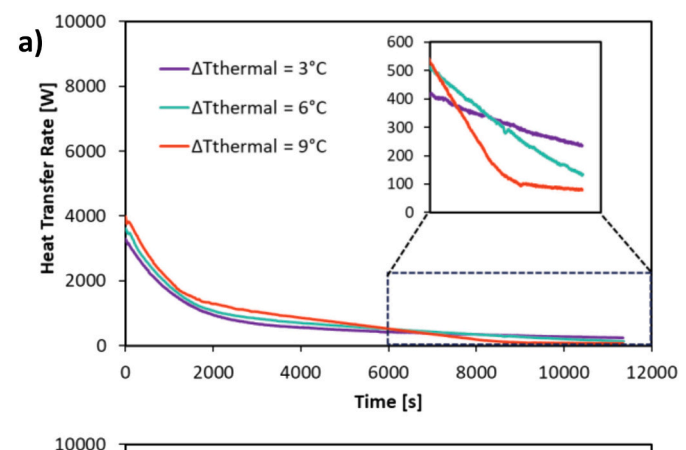
from 3 °C to 9 °C results in a reduction of about 50 %, from 6755 s to 3390 s. Similarly, for any given $\Delta T_{thermal}$, increasing the mass flow rate consistently reduces the melting time because higher flow rates deliver more thermal energy per unit time and result in higher HTC values realized inside the HTF channels. Regardless of $\Delta T_{thermal}$, raising the HTF flow rate from 100 to 150 kg h⁻¹ shortened the melting time by roughly 22 %, while increasing it from 100 to 200 kg h⁻¹ yielded larger reductions of about 35 %. These results are in agreement with the literature [38–40].

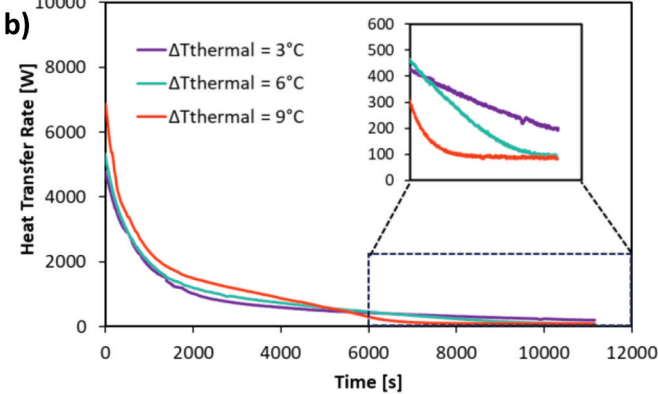
However, while both higher $\Delta T_{thermal}$ and increased mass flow rate are beneficial for reducing melting time, they come with trade-offs. Specifically, higher flow rates demand more pumping power and, thus, energy consumption, and may reduce overall system efficiency. With regards to the $\Delta T_{thermal}$, it strongly depends on the available energy source used to charge the LTES unit. Moreover, it must be considered that excessively high $\Delta T_{thermal}$ values are associated with increased thermal losses to the environment and increased exergy losses.

The heat transfer rate over time for the charging experiments at three different temperature differences ($\Delta T_{thermal} = 3$, 6, and 9 °C) is presented in Fig. 7. The heat transfer rate serves as a critical factor in how efficiently the HTF releases heat to the PCM during the charging process. In Fig. 7a), at the lowest flow rate equal to 100 kg h^{-1} , the maximum heat transfer rate reaches 4 kW for $\Delta T_{thermal}$ of 9 °C at the beginning of the charging process, then declines rapidly over time. Initially, the large temperature gradient between the HTF and the PCM leads to rapid sensible heat absorption, corresponding to the steep early heat transfer. After the first 2000 s, the temperature difference diminishes as the PCM heats up and begins to melt, causing a progressive reduction in heat transfer rate. For $\Delta T_{thermal} = 9$ °C, the heat transfer rate progressively reduces until stabilizing around 100 W by 9800 s, reflecting the slowing of heat transfer as the PCM approaches complete charging, as the temperature gradient becomes minimal. Steady-state conditions are reached after approximately 3.7 h for $\Delta T_{thermal}$ of 3 °C, 3.5 h for $\Delta T_{thermal}$ of 6 °C, and 2.7 h for $\Delta T_{thermal}$ of 9 °C, confirming the inverse relationship between $\Delta T_{thermal}$ and total charging duration discussed in Figs. 5 and 6. The insert in each Figure provides a magnified view of the later charging

Fig. 7b) illustrates similar trends for a flow rate of 150 kg h^{-1} . Initially, all $\Delta T_{thermal}$ trends exhibit high heat transfer rates, rapidly decreasing as the temperature gradient decreases and the melting process proceeds. The case with $\Delta T_{thermal} = 9~^{\circ}\text{C}$ results in the highest initial heat transfer rate (6.9 kW), followed by 6 $^{\circ}$ C (5.3 kW) and 3 $^{\circ}$ C (4.8 kW); as time progresses, the heat transfer rate gradually declines due to a reduction in the temperature gradient between the HTF and PCM, as well as the gradual completion of the phase change process. Notably, it is widely agreed that PCM-based thermal storage systems are never fully charged during normal operations, as the time required to store the final fraction of energy increases exponentially with the ever-decreasing heat transfer rate [26,41]. For example, between 6000 and 8000 s, the heat flow rate stabilizes and reaches a steady state condition. In this condition, the system has already reached a high state of charge, storing approximately 8233 kJ of energy (based on Eqs. (7) and (8)). Steadystate is reached more quickly than at 100 kg h⁻¹. Specifically, it is reached after about 3.6 h at $\Delta T_{thermal} = 3$ °C, 3 h at $\Delta T_{thermal} = 6$ °C, and 2 h at $\Delta T_{thermal} = 9$ °C.

In Fig. 7c), at a maximum flow rate of 200 kg h⁻¹, the initial heat transfer rate reaches around 9 kW for $\Delta T_{thermal} = 9$ °C, more than double the rate of 100 kg h⁻¹. However, the rate again declines steeply, reaching about 100 W by 7400 s. The experiment was terminated at this point, as further charging offered limited insight. Consequently, the time required for achieving steady-state conditions is shortest: 2.8 h for Δ $T_{thermal}$ of 3 °C, 2.3 h for $\Delta T_{thermal}$ of 6 °C, and 2 h for $\Delta T_{thermal}$ of 9 °C. Across all three cases, the starting heat transfer rate increases with the temperature difference $\Delta T_{thermal}$, with the highest values observed at Δ $T_{thermal}$ of 9 °C. This highlights a fundamental trade-off in the charging process: higher flow rates and larger temperature differences result in





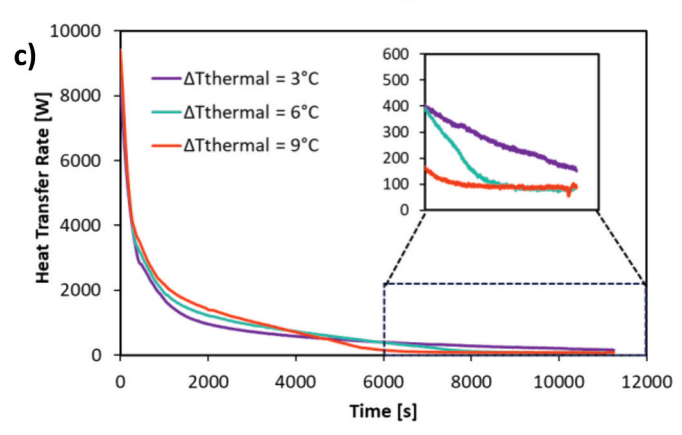


Fig. 7. Heat transfer rate as a function of time for charging experiments performed with the finned LTES unit: a) 100 kg h^{-1} , b) 150 kg h^{-1} , c) 200 kg h^{-1} .

faster energy transfer and shorter total charging time, but they also shorten the duration over which effective energy transfer occurs. In contrast, lower flow rates extend the heat transfer period, leading to a more gradual charging process, which could be desirable depending on the system's operational requirements.

The energy released by the heat transfer fluid and stored by the PCM and aluminum structure was calculated using Eqs. (6)–(8). Across a range of mass flow rates, initial PCM temperatures, and HTF inlet temperatures, the finned LTES unit demonstrated the ability to store energy between 7663 kJ and 8233 kJ. These values correspond to the minimum and maximum stored energy, respectively, and reflect the system's ability to effectively store thermal energy under varying operating conditions. For comparison, a sensible energy storage system of the same size, filled with water (about 34 kg) and working under the same HTF conditions, would be able to store up to about 6400 kJ, roughly 20 % less compared to the LTES unit.

On the other hand, the charging cycle efficiency was evaluated using

Eq. (14), defined as the ratio of energy stored in the PCM and aluminum to the energy released by HTF. The resulting efficiency ranged between 79 % and 87 %, depending on the test conditions.

$$\eta = \frac{\text{Energy stored by PCM and aluminum}}{\text{Energy released by HTF}} \cdot 100 \tag{14}$$

The relatively high efficiency underscores the effectiveness of the finned unit in storing thermal energy, with the fin design playing an essential role in improving the heat transfer and storage process. The maximum efficiency of 87 % was achieved at the highest mass flow rate (200 kg h $^{-1}$) and $\Delta T_{thermal}$ (9 °C), indicating that the LTES unit is most effective in storing thermal energy under these operating conditions. Notably, the efficiency of the LTES unit depends on several factors, including the thermophysical properties of the PCM, mass flow rate, temperature difference, ambient temperature, the initial PCM temperature at the start of the test and heat losses to the surroundings, all of which impact the system's overall performance.

3.2. Comparison between finned and finless LTES units

In Fig. 8, a comparison of finned and finless units during the charging process is presented at a mass flow rate of 200 kg h⁻¹ and $\Delta T_{thermal}$ of 9 °C. The Figure illustrates the temperature profiles of PCM and HTF versus time, where the PCM temperature of each zone represents the average value among the thermocouple measurements within that zone. In Fig. 8a), which depicts the results obtained with the finned unit, the PCM experiences a rapid temperature rise across all zones, especially during the early stage of the charging process, due to a higher heat transfer rate. The temperature profiles show that the PCM closest to the HTF inlet (zone 1) reaches the lower melting temperature faster than zones more distant from the inlet. As time progresses, all zones eventually reach a steady state condition, following the typical three-stage heating pattern: sensible heating in the solid phase, latent heat absorption during phase change, and sensible heating in the liquid phase. The presence of fins improves the heat exchanged by increasing the effective heat transfer surface area, promoting more uniform and faster PCM charging across all zones.

Conversely, Fig. 8b) presents the temperature profiles for the finless unit, where the heat transfer occurs at a much slower rate compared to the finned unit due to the absence of aluminum fins. This results in a more gradual temperature rise and a delayed occurrence of phase change in the finless unit, resulting in a longer time to reach a steady state condition compared to the finned unit.

The effect of fin integration is clearly demonstrated in the charging duration and energy storage performance. The finned unit completes the charging process in almost 2 h, whereas the finless unit requires nearly 8 h, demonstrating a fourfold reduction in charging time due to the presence of fins. The vertical red line in both graphs marks the point at which the temperature of the PCM in all zones and the HTF temperatures are within 1 K, indicating that the system has achieved a nearly uniform temperature distribution. It is interesting to note that, after a period of 7400 s at the flow rate of 200 kg h⁻¹ and $\Delta T_{thermal} = 9$ °C, the finned unit stores 7990 kJ of thermal energy (i.e., it is almost completely charged), while the finless unit has accumulated 2200 kJ. This highlights the significant role of fins in enhancing thermal performance and accelerating the charging process of the LTES units. Overall, these results demonstrate that the finned design may offer superior responsiveness, shorter melting time, and more complete exploitation of the PCM storage potential for applications requiring rapid and repeated thermal cycling.

Fig. 9a) compares the melting times of the finned and finless LTES units at a constant mass flow rate (200 kg h⁻¹) across three temperature differences ($\Delta T_{thermal}$ of 3 °C, 6 °C, and 9 °C). The graph illustrates a significant difference in the melting time between the two configurations. The finless unit exhibits considerably longer melting times across all temperature differences, highlighting its lower thermal performance.

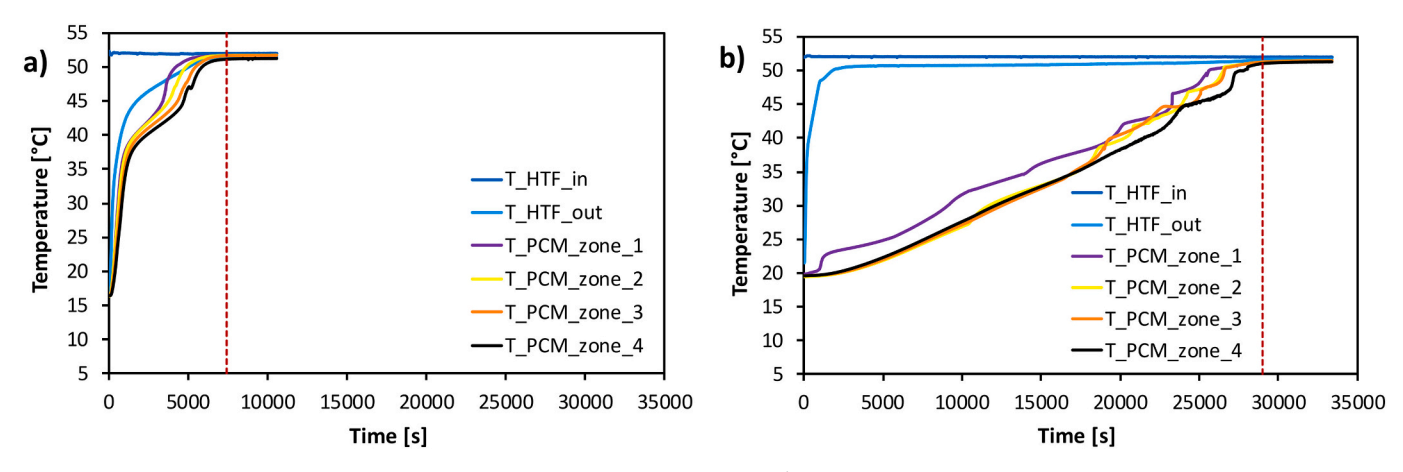


Fig. 8. Comparison of finned and finless units' temperature profiles at 200 kg h⁻¹ flow rate with $\Delta T_{thermal} = 9$ °C: a) finned unit, b) finless unit.

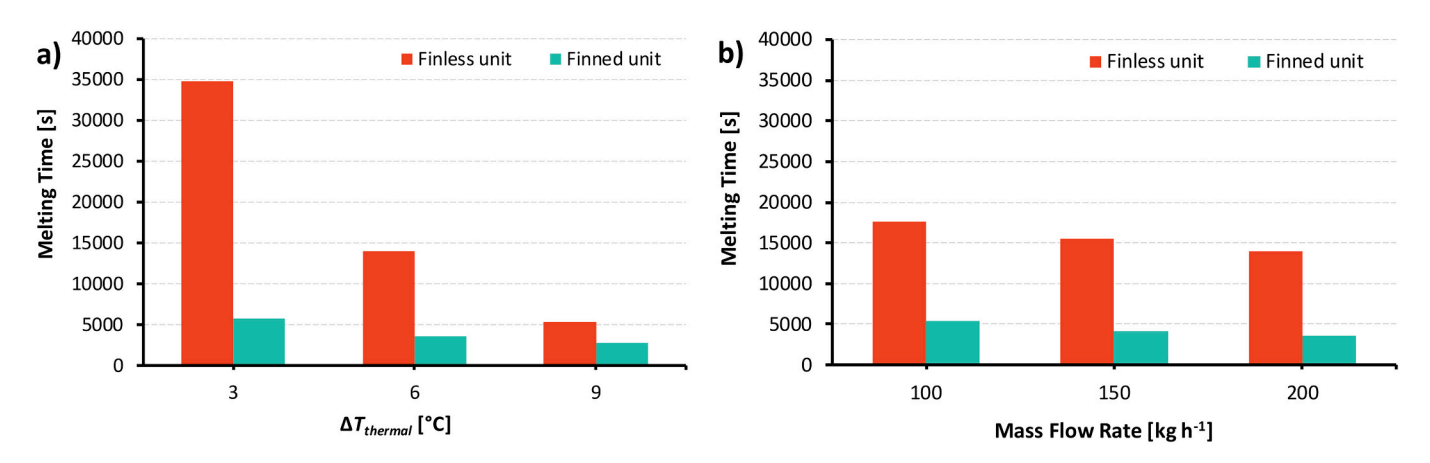


Fig. 9. Comparison of finned and finless units according to melting time: a) $\Delta T_{thermal}$ equal to 3 °C, 6 °C and 9 °C at 200 kg h⁻¹ mass flow rate; b) mass flow rate equal to 100 kg h⁻¹, 150 kg h⁻¹, and 200 kg h⁻¹ at $\Delta T_{thermal}$ of 6 °C.

An increase in $\Delta T_{thermal}$ significantly reduces the melting time for both configurations. However, fins in the finned unit substantially enhance the phase change process, as evidenced by considerably lower melting times than the finless unit. At $\Delta T_{thermal}=3$ °C, the finless unit takes 34700 s to complete the charging process, while the finned unit completes the process in just 5700 s, resulting in an 84 % reduction in the melting time for the finned unit. When $\Delta T_{thermal}$ increases to 6 °C, the finless unit's melting time drops to 13900 s, while the finned unit requires only 3600 s (74 % reduction). At the highest temperature difference of $\Delta T_{thermal}=9$ °C, the melting times for the finless and finned units further decrease to 5390 s and 2695 s, respectively (50 % reduction for the finned unit).

Fig. 9b) illustrates the effect of mass flow rate on melting time at a fixed $\Delta T_{thermal}$ of 6 °C, considering three mass flow rates (100, 150, 200 kg h $^{-1}$). In both finned and finless configurations, increasing the flow rate reduces melting time, as higher flow rates result in enhanced convective heat transfer coefficients at the HTF side and more uniform temperature distribution along the water flow direction. Specifically, when the flow rate increases from 100 to 200 kg h $^{-1}$, the melting time decreases by approximately 22 % (from 17650 s to 13940 s) for the finless unit and 34 % (from 5445 s to 3590 s) for the finned unit. Interestingly, the ratio of melting time between the two configurations remains almost constant (at about 28 %) for all the flow rate conditions. This indicates that forced convection on the HTF side exerts the same effect on both units.

From Fig. 9, it can be concluded that a higher temperature difference generally enhances heat transfer, resulting in shorter melting times, which holds true for both the finned and finless units. In the finned unit,

the melting time shows an almost linear trend with the temperature difference. This could be explained considering the dominant effect of thermal conduction on the heat transfer rate in the LTES unit. Natural convection is not expected to exert a significant influence as the PCM is confined within narrow cavities enclosed by fins. On the other hand, in the finless unit, the melting time displays a non-linear dependence on the temperature difference. Indeed, thermal conduction and natural convection are both present and act concurrently to the overall heat transfer [42,43].

4. Numerical modeling of the LTES unit

4.1. Model description

A numerical model of the LTES unit was developed in MATLAB® environment to study the thermal behaviour under different operating conditions. The system has been modeled using a resistance-capacitance (RC) approach, assuming constant thermophysical properties in each node. Considering the presented LTES unit, there are three principal media where heat transfer occurs, corresponding to different discretization types: water, container (aluminum), and PCM+fins assembly. A schematic of the discretized domain, considering the different materials, is reported in Fig. 10. The Figure depicts the LTES unit's top view, subdivided into 9 rows and 31 columns matrix, whose PCM elements have a 4 cm square cross-section. This element size was selected to ensure numerical accuracy, with deviations below 1 % compared to finer grids, while maintaining an acceptable computational time. The total discretization consists of two stacked matrices of the same size: the

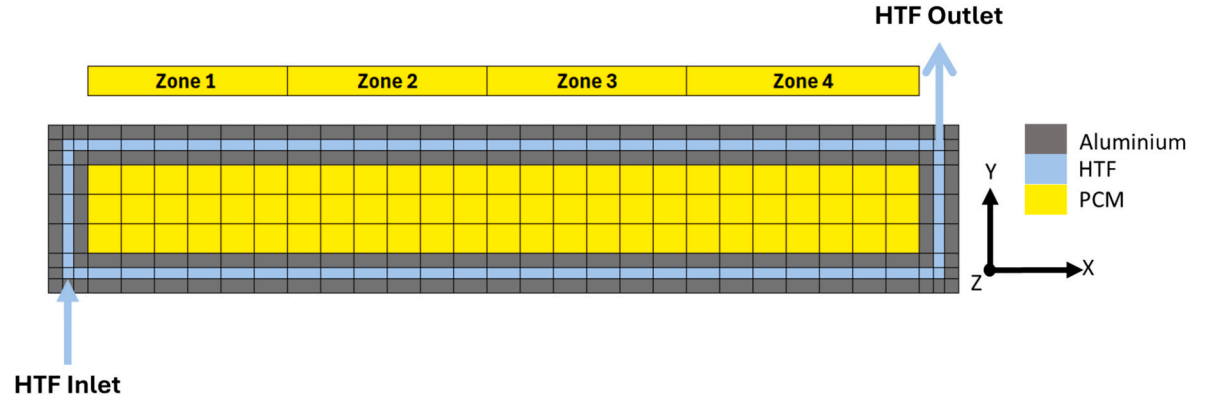


Fig. 10. Nodal discretization of LTES unit (top view).

vertical length of the top discretization is 31 cm (Fig. 10), whereas the vertical length of the bottom discretization is 0.5 cm (equal to the bottom container thickness). The top matrix contains aluminum elements (136 nodes), water elements (87 nodes), and PCM+fins elements (75 nodes), whereas the bottom matrix contains only aluminum elements (279 nodes).

In the present model, the following assumptions are made:

- The heat transfer towards the environment is neglected (as experiments confirmed their influence to be negligible),
- Natural convection is neglected in the liquid PCM. Fins are assumed to limit this phenomenon [44,45],
- The heat capacity of water is neglected: thermal inertia is assumed to be negligible compared to convection.

The effect of natural convection during PCM melting was disregarded in the present model due to the limited spacing between adjacent aluminum fins (<1 cm). This assumption is consistent with previous studies where the contribution of convection in confined PCM geometries was found to be negligible. For example, Stathopoulos et al. [44] adopted the same simplification in the numerical model of an air-PCM plate-and-fin heat exchanger with cavity dimensions (1000 mm \times 200 mm \times 18 mm) much larger than those considered in the present work. Similarly, Zivkovic and Fujii [46] validated a computational model of a rectangular container (100 mm × 100 mm × 20 mm), concluding that, for the considered flat thin container, the effects of natural convection within the liquid PCM could be ignored without introducing a significant error in the prediction of the temperature variation with time within the PCM. Neumann et al. [45] also neglected the contribution of natural convection in the simulation of a fin-andtube heat exchanger with paraffin, owing to the small distance between fins (5 mm). More recently, Berto et al. [10] reported the same assumption for a latent TES integrated with an evaporator for a compressed air dryer. The PCM enclosure had a fin spacing of 9 mm and a fin height of 12 mm.

In the present LTES unit, the height of the PCM fins is 12 mm and the fin spacing is 8 mm, dimensions comparable to or smaller than those considered in the cited works. Given these geometric constraints and the thermophysical properties of paraffin-based PCMs, the effect of natural convection can be reasonably regarded as negligible.

Each element is modeled with a heat balance equation that depends on its material and that of the adjacent elements. A generic node of aluminum and PCM (including the liquid PCM) is described by the unsteady energy conservation equation arising from the application of Fourier's law:

$$\rho \cdot V \cdot c \cdot \frac{\left(T_{ijk}^{r+1} - T_{ijk}^{r}\right)}{\Delta \tau} = \frac{\Delta y \cdot \Delta z}{R_{x+}} \cdot \left(T_{i+1jk}^{r+1} - T_{ijk}^{r+1}\right) + \frac{\Delta y \cdot \Delta z}{R_{x-}} \cdot \left(T_{i-1jk}^{r+1} - T_{ijk}^{r+1}\right) + \frac{\Delta x \cdot \Delta z}{R_{y+}} \cdot \left(T_{ij+1k}^{r+1} - T_{ijk}^{r+1}\right) + \frac{\Delta x \cdot \Delta z}{R_{y-}} \cdot \left(T_{ij-1k}^{r+1} - T_{ijk}^{r+1}\right) + \frac{\Delta x \cdot \Delta y}{R_{z\pm}} \cdot \left(T_{ijk\pm 1}^{r+1} - T_{ijk}^{r+1}\right)$$

$$(15)$$

where implicit temporal discretization is used. In Eq. (15), i,j and k identify the nodes in the two horizontal (x,y) and vertical (z) directions and Δx , Δy , Δz represent the distance between the nodes. The subscripts of the generic thermal resistances R are defined accordingly. In Eq. (15), there is only one term referring to the nodes along z, since only two discretizations are realized in the vertical direction.

In the PCM domain, a simplified version of the so-called effective specific heat method [47] is used to account for the phase change. In the process, an apparent specific heat capacity c_{PCM} is used in the phase change temperature range:

$$c_{PCM,eff} = \begin{cases} c_{PCM,l} & T_{i,j,k}^{r+1} > T_{up_melt} \\ \frac{\Delta h}{\Delta T_{melt}} & T_{low_melt} < T_{i,j,k}^{r+1} < T_{up_melt} \\ c_{PCM,s} & T_{i,j,k}^{r+1} < T_{low_melt} \end{cases}$$

$$(16)$$

In the heat transfer fluid elements, an advection term is also considered. For a generic HTF node surrounded by two aluminum nodes in which the fluid flows along the x direction, it results:

$$\dot{m}_{HTF,ch} \cdot c_{HTF} \cdot \left(T_{i+1j,k}^{r+1} - T_{ij,k}^{r+1} \right) = \frac{\Delta x \cdot \Delta z}{R_{y+}} \cdot \left(T_{ij+1,k}^{r+1} - T_{ij,k}^{r+1} \right) + \frac{\Delta x \cdot \Delta y}{R_{y-}} \cdot \left(T_{i,j-1,k}^{r+1} - T_{ij,k}^{r+1} \right) \\
- T_{i,j,k}^{r+1} + \frac{1}{R_{z-}} \cdot \left(T_{i,j,k-1}^{r} - T_{i,j,k}^{r+1} \right) \tag{17}$$

where $\dot{m}_{HTF,ch}$ is the flow rate of HTF in the channel. In Eqs. (15) and (17) the total thermal resistance depends both on the materials between two nodes and the direction of the heat flow. In the case of HTF discretization, the total resistance is calculated as a series between the thermal resistance due to conduction through the aluminum wall, and the resistance due to the HTF flow in the channel:

$$R_{HTF-wall} = \frac{1}{\frac{\lambda_{al}}{w_{sh}} + \alpha_{HTF}}$$
 (18)

where λ_{al} is the thermal conductivity of aluminum, w_{th} is the wall

thickness and α_{HTF} is the convective heat transfer coefficient on the HTF side. The latter is calculated according to Eq. (19):

$$\alpha_{HTF} = \frac{\text{Nu} \cdot \lambda_{HTF}}{D_h} \tag{19}$$

where Nu is the Nusselt number, calculated as follows:

$$Nu = j \cdot Re \cdot Pr^{\frac{1}{3}}$$
 (20)

In Eqs. (19) and (20) the hydraulic diameter D_h , Colburn factor j, Reynolds number and Prandtl number are calculated using Eqs. (21)–(26) as a function of the geometry of the off-strip fins (Figure 11) and the mass flow rate of the HTF in the channel [48,49]:

$$A = H \cdot (1 - n \cdot t) \cdot L \tag{21}$$

where n is the number of off-strip fins per unit length, t is the thickness of the fins, H is the fins' height and L is the HTF channel width. The fin spacing s and the fin length l are also considered in the definition of the hydraulic diameter:

$$D_h = \frac{2 \cdot (s-t) \cdot H}{\left[(s-t) + H + \frac{H \cdot t}{l} \right]}$$
 (22)

$$Re = \frac{\dot{m} \cdot D_h}{A \cdot \mu} \tag{23}$$

$$Pr = \frac{c \cdot \mu}{\lambda} \tag{24}$$

If Re > 1500 :

$$j = 0.21 \cdot \text{Re}^{-0.4} \cdot \left(\frac{l}{D_h}\right)^{-0.24} \cdot \left(\frac{t}{D_h}\right)^{0.02}$$
 (25)

If Re < 1500:

$$j = 0.53 \cdot \text{Re}^{-0.5} \cdot \left(\frac{l}{D_h}\right)^{-0.15} \cdot \left(\frac{s}{H}\right)^{-0.14}$$
 (26)

In the PCM + fins domain, the thermal resistances have been determined as a function of an apparent thermal conductivity λ_{app} , calculated assuming that the fins are rectangular, according to Figs. 11 and 12. Given the high thermal conductivity of aluminum compared to the PCM, the calculation of the apparent thermal conductivities has been realized considering the length and thickness of the aluminum fins and plate along the x and y direction.

$$R_{PCM,x} = \frac{\lambda_{app,x}}{\Delta x} \tag{27}$$

$$R_{PCM,y} = \frac{\lambda_{app,y}}{\Delta y} \tag{28}$$

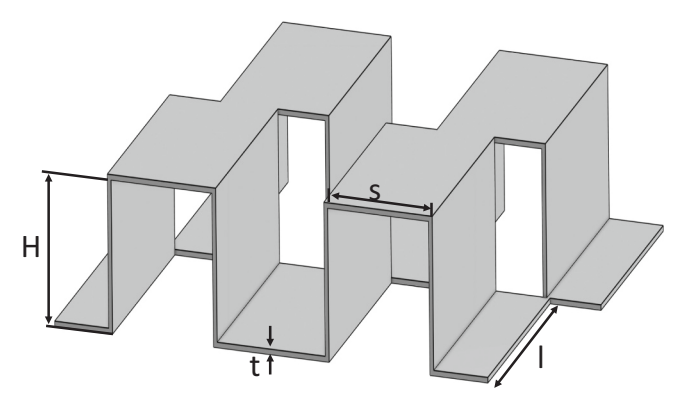


Fig. 11. Scheme of the off-strip fins inside the HTF channel.

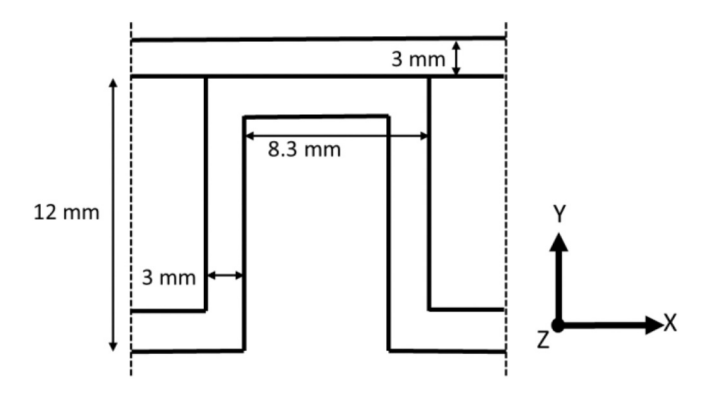


Fig. 12. PCM element view from the top, considered for the calculation of the apparent thermal conductivity.

The solution procedure, summarized in the flowchart (Fig. 13), begins with the definition of the system geometry, material properties, and the initial temperatures of both the PCM and the wall. The inlet temperature and mass flow rate of the HTF are also fixed. The model adopts a fully implicit finite-difference scheme to evaluate nodal temperatures. At each time step, nodal values are updated according to Eqs. (15)–(17), and the net heat flux exchanged with adjacent nodes is computed. This heat flux represents the total heat released or absorbed by the material in the node. The fluxes are then summed to verify energy conservation within the domain. If the cumulative imbalance exceeds a predefined tolerance (i.e., 0.1 W), the iteration is repeated using the updated temperatures with an under-relaxation factor to improve numerical stability. If the condition is satisfied, the solution advances to the next time step.

A time step of 5 s was selected as the optimal compromise between computational effort (which would benefit from higher time step) and model accuracy (which would benefit from smaller time step), leading to numerical deviations in melting time predictions below 0.1 %.

4.2. Validation of the model

The experimental database obtained with the finned unit at different temperature differences ($\Delta T_{thermal}$) and mass flow rates were used to validate the proposed model. The model inputs are listed in Table 3. Fig. 14a) shows the experimental and calculated temporal evolution of average temperature profiles in the PCM cavity for three temperature differences of 3, 6, and 9 °C at a flow rate of 200 kg h $^{-1}$. The PCM temperature was obtained by averaging the values recorded by the zonal thermocouples positioned in the unit's central axis. As expected, the case with a temperature difference of 9 °C accelerates the charging process, reaches a steady state condition more quickly. In this case, the system approaches a near steady state at approximately 6000 s. The calculated profiles (dashed lines) align closely with the experimental data (solid lines), demonstrating the model's accuracy in predicting the overall thermal response of the PCM during the charging process.

In addition to the zone-averaged validation (Fig. 14a), a quasi-local validation was performed by comparing experimental and numerical PCM average temperatures along the central axis in two representative regions (Zones 1 and 4). Such comparison is shown in Fig. 14b), where the experimental values for Zone 1 and Zone 4 are respectively the average of the measurements from thermocouples 5–8 and 29–32, while the numerical counterparts are calculated as the average of the two computational nodes located at almost the same positions as the thermocouples. The predicted profiles show very good agreement with the measurements, with maximum deviations below 1 K. This corroborates that the model can reproduce not only the zone-averaged behaviour shown in Fig. 14a), but also quasi-local temperature dynamics at distinct positions, thereby strengthening confidence in its predictive capability.

The experimental and calculated melting times at varying $\Delta T_{thermal}$

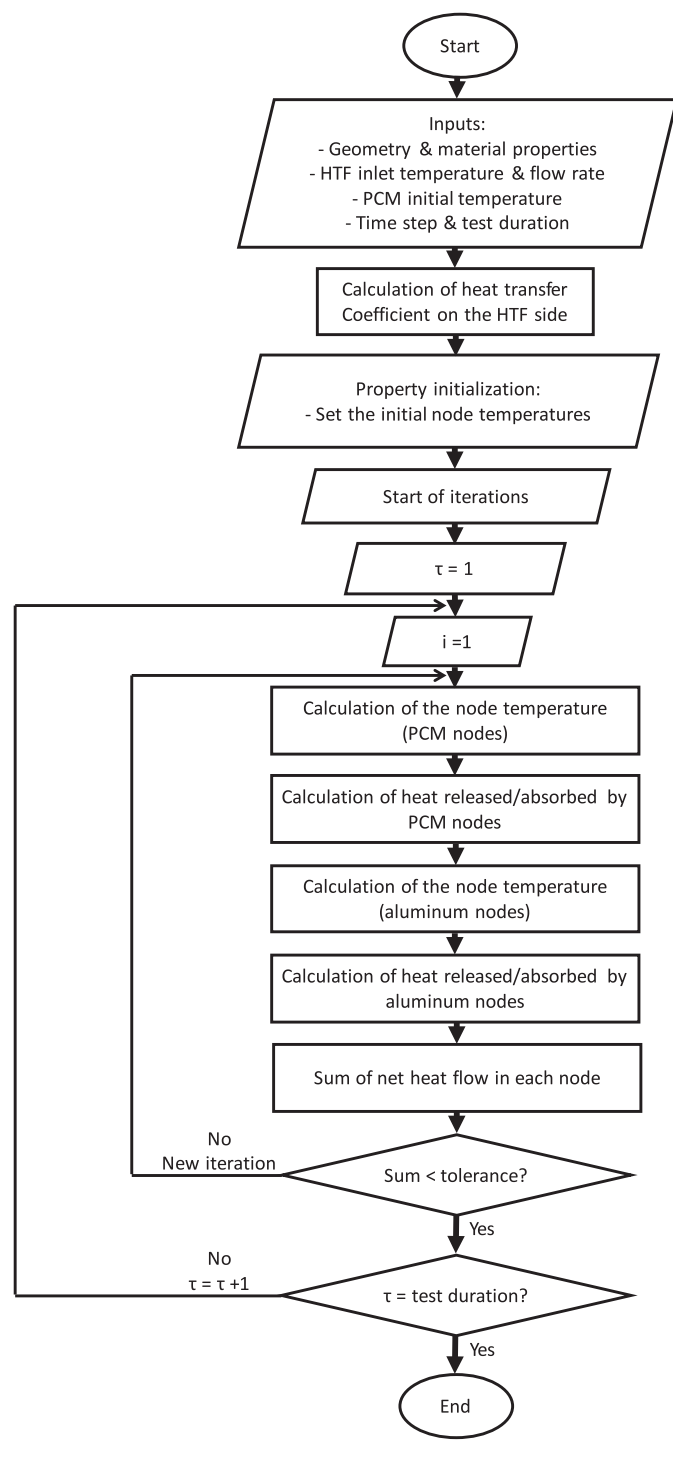


Fig. 13. Block diagram of the model resolution algorithm.

(3, 6, and 9 °C) and flow rates (100, 150, and 200 kg h $^{-1})$ are reported in Fig. 15. The melting time was calculated using Eq. (13), as the time difference between the lower melting temperature reached in Zone 1 and the upper melting temperature reached in Zone 4. The markers on the graph represent the melting time for each case, while the error bars (dashed lines) indicate a \pm 10 % uncertainty. The data points align closely with the bisector line, with a maximum relative deviation between calculated and experimental values of 6 %.

Table 3Model inputs.

Parameters	Value		
Aluminum specific heat [J kg ⁻¹ K ⁻¹]	903		
Aluminum thermal conductivity [W m ⁻¹ K ⁻¹]	185		
Aluminum density [kg m ⁻³]	2750		
Aluminum wall thickness [m]	0.005		
PCM thermal conductivity [W m ⁻¹ K ⁻¹]	0.26		
PCM fin thickness [m]	0.0003		
PCM fin pitch [m]	0.0083		
PCM fin height [m]	0.012		
PCM cavity width [m]	0.12		
HTF channel thickness [m]	0.003		
HTF fin thickness [m]	0.0002		
HTF fin pitch [m]	0.003		
HTF fin height [m]	0.003		
HTF fin length [m]	0.005		
HTF flow rate [kg h ⁻¹]	100, 150, 200		
HTF temperature at inlet [°C]	46, 49, 52		
Time step [s]	5		
Total simulation duration [s]	Until it reaches steady state		

4.3. Parametric study to find optimal geometries

Once the numerical model was validated, it was employed for parametric studies to analyze the effect of various factors, such as the geometry of the finned surface within the PCM cavity, on the performance of the LTES unit. Specifically, the study focused on the influence of fin thickness, height and pitch on key performance metrics, including melting time and stored energy. The thermal conduction in the LTES unit is enhanced by the aluminum finned surface, whose geometrical parameters dictate the system's heat transfer efficiency. Hence, examining the effect of these geometrical parameters on the model output is worthwhile. Table 4 summarizes the results of the parametric study, highlighting how fin geometry variations affect melting time and stored energy. The analysis uses a reference case as the baseline, with fin thickness, height and pitch set at 0.03 cm, 1.2 cm, and 0.83 cm, respectively.

The fin thickness was varied from 0.03 cm (reference case) to 0.06 cm, 0.09 cm, and 0.12 cm. As shown in Table 4, increasing fin thickness (e.g., cases 8, 15, and 22) reduces the PCM mass due to the increased volume occupied by the fins, with a reduction of the PCM mass from 27 kg (reference case) to 24.8 kg, 22.8 kg, and 21 kg in cases 8, 15, and 22, respectively. Additionally, thicker fins significantly enhance heat conduction, leading to shorter melting times. For example, with a thickness of 0.12 cm (case 22), the melting time is reduced to 1675 s compared to 2675 s in the reference case. However, thicker fins result in lower stored energy due to the reduced PCM mass (6369 kJ for case 22 compared to 7066 kJ in the reference case).

The effect of varying fin height was examined using 0.6 cm, 1.2 cm (reference case), 1.8 cm, and 2.4 cm. The results indicate that increasing fin height (e.g., cases 1, 2, and 3) slightly increases PCM mass, as taller fins occupy less lateral space, allowing more PCM to be accommodated in the cavity. For example, PCM mass increases from 27 kg in the reference case to 27.5 kg and 27.8 kg in cases 2 and 3, respectively. In comparison, taller fins result in slower heat transfer, leading to longer melting times compared to the reference case (e.g., from 2675 s for the reference case to 3035 s for case 2 and 3355 s for case 3). Despite the longer melting times, taller fins slightly enhance stored energy due to the higher PCM mass. For example, stored energy increases from 7066 kJ (reference case) to 7144 kJ in case 3.

The analysis also explored fin pitches of 0.42 cm, 0.56 cm, 0.83 cm (reference case), and 1.67 cm. As reported in Table 4, decreasing fin pitch (e.g., cases 4, 5, and 6) increases the number of fins and reduces the PCM mass within the PCM cavity. For instance, PCM mass decreases from $27.5 \, \text{kg}$ (case 4) to $25 \, \text{kg}$ (case 6) as pitch decreases from $1.67 \, \text{cm}$ to 0.42 cm. A smaller pitch improves heat transfer due to the increased overall heat transfer area, resulting in shorter melting times, as the

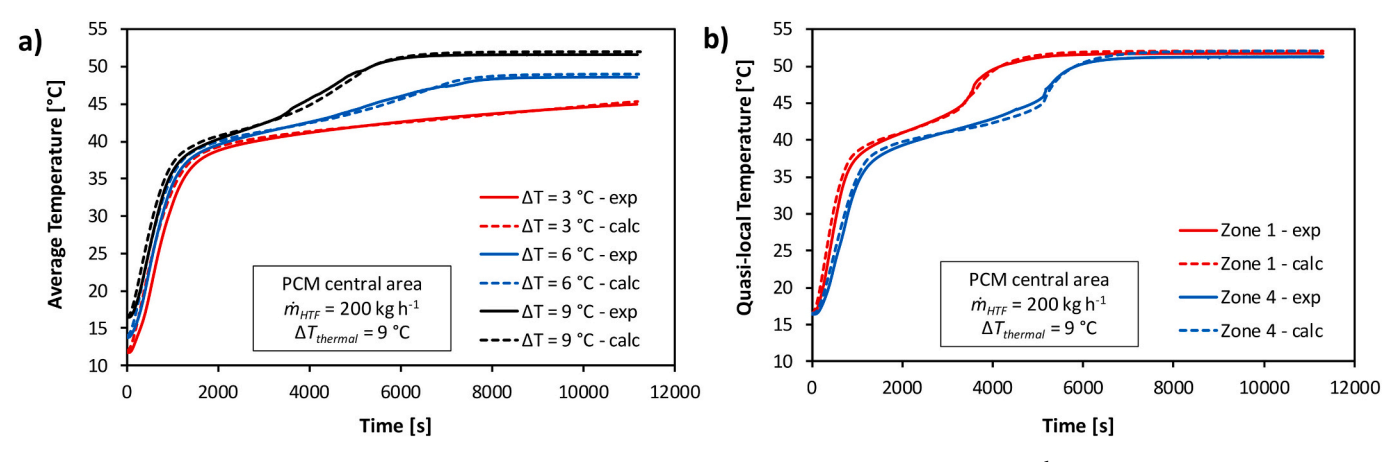
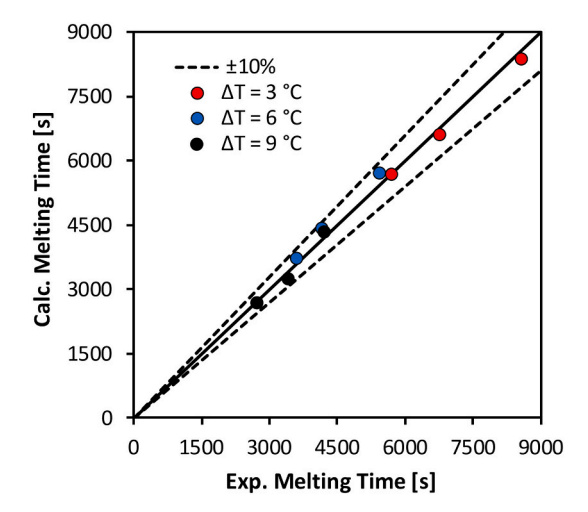


Fig. 14. a) Comparison between experimental and calculated average PCM temperatures at mass flow rate of 200 kg h⁻¹ and $\Delta T_{thermal}$ of 3, 6, and 9 °C; b) comparison between experimental and calculated quasi-local PCM temperatures in Zones 1 and 4 considering the central area of the unit, at mass flow rate of 200 kg h⁻¹ and $\Delta T_{thermal}$ of 9 °C.



 $\begin{tabular}{ll} \textbf{Fig. 15.} & \textbf{Comparison of melting time between experimental and calculated results.} \end{tabular}$

closer spacing of fins improves heat conduction. For instance, at a pitch of 0.42 cm (case 6), the melting time is 2025 s compared to 2675 s in the reference case. However, a smaller fin pitch reduces the available space for PCM mass, leading to lower stored energy. For instance, stored energy decreased from 7130 kJ in case 4 to 6871 kJ in case 6.

The observed trade-off between PCM mass, melting time, and stored energy suggests that cases with higher PCM mass, such as case 3 (27.8) kg), show longer melting time (3355 s) but higher stored energy (7144 kJ). Conversely, cases with lower PCM mass, such as case 27 (17 kg), demonstrate shorter melting times (1425 s) but lower stored energy (5965 kJ). The design choices are driven by the trade-off between maximizing stored energy and minimizing melting time. If the primary goal is to maximize stored energy, configurations like Case 3 (fin thickness: 0.03 cm, fin height: 2.4 cm, fin pitch: 0.83 cm) are optimal, as they provide the highest stored energy (7144 kJ). On the other hand, if the priority is faster melting time with a reasonable amount of stored energy, configurations like Case 6 (fin thickness: 0.03 cm, fin height: 1.2 cm, fin pitch: 0.42 cm) are better, achieving a much faster melting time (2025 s) while still storing 6871 kJ of energy. Designers may adjust these parameters based on their specific application needs – whether it requires higher energy storage or faster melting time.

Fig. 16 illustrates the relationship between the melting time and the specific stored energy (kWh $\rm m^{-3}$) in a thermal storage system, with data from Table 4 plotted as blue circles. A third-order polynomial regression

fitted to the data, shown as a dotted line, achieves an R² value of 0.98, demonstrating excellent agreement with the simulated data.

The numerical results emphasize that the thermal storage system performance depends on balancing specific stored energy and melting time. Larger fin height and moderate fin pitch enhance stored energy but prolong melting times, while designs with smaller fin pitches and reduced fin height shorten melting time but reduce energy storage. The regression model confirms that optimizing one parameter inherently impacts the other, making it crucial to select design parameters based on the application's specific needs, whether prioritizing maximum energy storage or faster melting time.

5. Conclusions and future work

This study presented a comprehensive experimental and numerical investigation of bar-and-plate latent thermal energy storage (LTES) units, comparing finned and finless configurations during charging under different conditions of heat transfer fluid mass flow rates (100, 150, 200 kg h $^{-1}$) and inlet temperatures (46, 49, and 52 $^{\circ}$ C). The key findings are summarized as follows:

- In the finned unit, the higher the $\Delta T_{thermal}$ and mass flow rate, the shorter the melting time. Increasing $\Delta T_{thermal}$ from 3 °C to 9 °C at 200 kg h⁻¹ reduced the melting time by 53 % (from 5705 s to 2695 s). Conversely, increasing the mass flow rate from 100 to 200 kg h⁻¹ at $\Delta T_{thermal} = 9$ °C, reduced melting time by 36 % (from 4185 to 2695 s). A maximum efficiency of 87 % was observed at the highest $\Delta T_{thermal}$ and mass flow rate, with the finned unit storing between 7663 kJ and 8233 kJ.
- Compared to the finless unit, the presence of fins resulted in a charging time reduction by up to 84 % under a temperature difference of 3 °C and a mass flow rate of 100 kg h⁻¹, with melting time decreasing from 34775 s (finless) to 5705 s (finned). Increasing the mass flow rate from 100 to 200 kg h⁻¹ further shortened the melting time by up to 36 % (5445 s to 3590 s). Overall, the finned unit completed charging in just 2 h compared to 8 h for the finless unit, at $\Delta T_{thermal}$ equal to 9 °C and mass flow rate of 200 kg h⁻¹.
- A numerical model of the LTES unit using a resistance-capacitance approach was developed and validated with experimental data, achieving high accuracy in predicting temperature profiles, heat transfer rate, melting times, and stored energy. In particular, the maximum deviation between experimental and numerical values of melting time was below 6 %.
- Parametric analysis of the effect of finned surface geometry on the LTES unit performance revealed significant trade-offs: larger fin height and moderate fin pitch increase stored energy but prolong

Table 4
Results of the parametric study. Effect of varying geometrical parameters (fin thickness, pitch, and height) on melting time and stored energy.

Case	Fin thickness [cm]	Fin height [cm]	Fin pitch [cm]	Melting time [s]	PCM mass [kg]	Stored energy [kJ]
Reference case	0.03	1.2	0.83	2675	27	7066
1	0.03	0.6	0.83	2185	26	6930
2		1.8	0.83	3035	27.5	7114
3		2.4	0.83	3355	27.8	7144
4		1.2	1.67	2750	27.5	7130
5		1.2	0.56	2155	26	6965
6		1.2	0.42	2025	25	6871
7		0.6	0.83	1830	22.8	6576
8		1.2	0.83	2135	24.8	6816
9		1.8	0.83	2340	25.6	6908
10	0.06	2.4	0.83	2505	26	6956
11		1.2	1.67	2185	25.8	6930
12		1.2	0.56	2020	24	6708
13		1.2	0.42	1915	23	6597
14		0.6	0.83	1605	20	6277
15		1.2	0.83	1865	22.8	6583
16		1.8	0.83	2015	24	6704
17	0.09	2.4	0.83	2135	24.4	6769
18		1.2	1.67	1970	24.2	6746
19		1.2	0.56	1735	21.5	6526
20		1.2	0.42	1625	20	6266
21		0.6	0.83	1445	18	6018
22	0.12	1.2	0.83	1675	21	6369
23		1.8	0.83	1815	22	6513
24		2.4	0.83	1915	23	6592
25		1.2	1.67	1830	23	6577
26		1.2	0.56	1545	19	6170
27		1.2	0.42	1425	17	5965

melting times, whereas designs with smaller fin pitches and reduced fin height accelerate melting but reduce energy storage. Thus, optimizing one parameter inherently affects the other, highlighting the need to select finned surface design according to the specific application requirements, whether prioritizing maximum energy storage or faster melting.

Overall, the present finned bar-and-plate LTES design allows to reach nearly 60 kWh $\rm m^{-3}$, enabling faster charge-discharge rates thanks to the extended surface area provided by the fins. Therefore, the present LTES system represents a compact and efficient solution for rapid thermal energy storage, offering significant advantages for applications requiring fast and repeated thermal cycling, such as domestic hot water and renewable energy integration.

Future research will focus on integrating the finned LTES unit in a

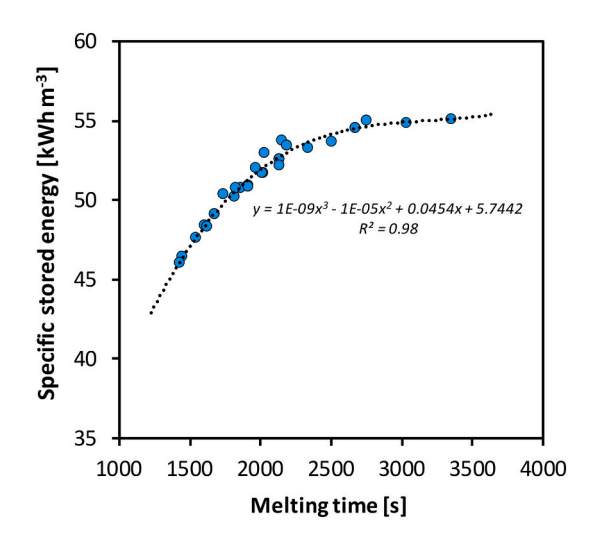


Fig. 16. Specific energy stored versus melting time results of the parametric study.

real energy system prototype for the conversion of the solar thermal energy. Additional efforts will include optimizing the fin geometry and applying dynamic HTF temperature profiles to better reproduce real operating conditions. Together, these studies are intended to improve the efficiency, durability, and practical deployment of finned LTES systems in renewable energy applications.

CRediT authorship contribution statement

Waseem Raza: Writing – review & editing, Writing – original draft, Methodology, Investigation, Formal analysis, Data curation. Marco Tancon: Writing – review & editing, Validation, Investigation, Data curation. Emanuele Zanetti: Writing – review & editing, Validation, Methodology, Investigation, Formal analysis. Arianna Berto: Writing – review & editing, Validation, Data curation. Stefano Rossi: Validation, Investigation. Marco Azzolin: Writing – review & editing, Supervision, Methodology, Conceptualization.

Declaration of competing interest

The authors declare the following financial interests/personal relationships which may be considered as potential competing interests:

Arianna Berto reports financial support was provided by European Commission. If there are other authors, they declare that they have no known competing financial interests or personal relationships that could have appeared to influence the work reported in this paper.

Acknowledgments

This study was developed in the framework of the research activities carried out within the Project "Network 4 Energy Sustainable Transition—NEST", Spoke 1, Project code PE0000021, funded under the National Recovery and Resilience Plan (NRRP), Mission 4, Component 2, Investment 1.3 – Call for tender No. 1561 of 11.10.2022 of Ministero dell'Università e della Ricerca (MUR); funded by the European Union – NextGenerationEU. This work has been also supported by MASE – ENEA

program "Ricerca di Sistema Elettrico – Piano Triennale di Realizzazione PTR 2022–2024 – Tecnologie per la penetrazione efficiente del vettore elettrico negli usi finali".

Data availability

Data will be made available on request.

References

- Goal 7 | Department of Economic and Social Affairs. https://sdgs.un.org/goals/goal7 (accessed August 4, 2025).
- [2] Paris Agreement Status of Ratification | UNFCCC. https://unfccc.int/process/the -paris-agreement/status-of-ratification (accessed August 16, 2024).
- [3] L.M. Nhut, W. Raza, Y.C. Park, A parametric study of a solar-assisted house heating system with a seasonal underground thermal energy storage tank, Sustainability 12 (2020) 8686, https://doi.org/10.3390/su12208686.
- [4] R. Conte, E. Zanetti, M. Tancon, M. Azzolin, S. Girotto, D. Del Col, The advantage of running a direct expansion CO2 heat pump with solar-and-air simultaneous heat sources: experimental and numerical investigation, Appl. Energy 369 (2024) 123478, https://doi.org/10.1016/j.apenergy.2024.123478.
- [5] D. MacPhee, I. Dincer, Performance assessment of some ice TES systems, Int. J. Therm. Sci. 48 (2009) 2288–2299, https://doi.org/10.1016/j. iithermalsci.2009.03.012.
- [6] X. Zheng, Z. Tang, Y. Wang, H. Liu, Performance of the air source heat pump assisted solar heating system combined with PCM floor, Appl. Therm. Eng. 239 (2024) 122115, https://doi.org/10.1016/j.applthermaleng.2023.122115.
- [7] X.Y. Zhang, Y.T. Ge, Burra, P.Y. Lang, Experimental investigation and CFD modelling analysis of finned-tube PCM heat exchanger for space heating, Appl. Therm. Eng. 244 (2024) 122731, https://doi.org/10.1016/j.applthermaleng.2024.122731.
- [8] S. Kim, R.A. Stavins, V.S. Garimella, E. Koronio, T. Shockner, G. Ziskind, N. Miljkovic, W.P. King, Cooling high power electronics using dynamic phase change material, Int. J. Heat Mass Transf. 237 (2025) 126433, https://doi.org/ 10.1016/j.ijheatmasstransfer.2024.126433.
- [9] X. Zhang, C. Yu, C. Zhang, Advances in latent heat storage technology for electronic cooling, Renew. Sustain. Energy Rev. 215 (2025) 115614, https://doi. org/10.1016/j.rser.2025.115614.
- [10] A. Berto, M. Azzolin, D. Del Col, Experimental and numerical study of an evaporator with integrated latent heat storage for a compressed air dryer, Appl. Therm. Eng. 195 (2021) 117170, https://doi.org/10.1016/j. applthermaleng.2021.117170.
- [11] S. Duraipandi, S. A., Investigation on the performance of a natural convection solar dryer with novel palmitic and sebacic acid eutectic phase change material for thermal energy storage applications, J. Energy Storage 77 (2024) 109908, https:// doi.org/10.1016/j.est.2023.109908.
- [12] K. Li, L. Shi, Y. Zhang, Y. Yao, C. Zhang, H. Tian, G. Shu, Study on electric vehicle thermal management system using phase change materials and CO2 heat pump waste heat recovery under cold conditions, Appl. Therm. Eng. 252 (2024) 123669, https://doi.org/10.1016/j.applthermaleng.2024.123669.
- [13] R. Li, Z. Wu, J. Luo, Z. Zou, Y. Huang, X. Zhou, G. He, Development and validation of a 200 kW PEM fuel cell system with a novel PCM-integrated waste heat recovery strategy, J. Energy Storage 122 (2025) 116697, https://doi.org/10.1016/j. est.2025.116697.
- [14] R. Bharathiraja, T. Ramkumar, L. Karthick, M. Mohanraj, Performance investigation on flat plate solar water collector using a hybrid nano-enhanced phase change material (PCM), J. Energy Storage 86 (2024) 111163, https://do. org/10.1016/j.est.2024.111163.
- [15] V. Goel, A. Dwivedi, R. Kumar, R. Kumar, A.K. Pandey, K. Chopra, V.V. Tyagi, PCM-assisted energy storage systems for solar-thermal applications: review of the associated problems and their mitigation strategies, J. Energy Storage 69 (2023) 107912, https://doi.org/10.1016/j.est.2023.107912.
- [16] B.K. Choure, T. Alam, R. Kumar, A review on heat transfer enhancement techniques for PCM based thermal energy storage system, J. Energy Storage 72 (2023) 108161, https://doi.org/10.1016/j.est.2023.108161.
- [17] B. Kurşun, M. Balta, F. Polat, Simultaneous evaluation of charge/discharge times and energy storage/release capacities in multi-tube latent heat energy storage with metal foam-enhanced PCM, J. Energy Storage 108 (2025) 115090, https://doi.org/ 10.1016/j.est.2024.115090.
- [18] V.K. Yadav, M. Jee, J. Sarkar, P. Ghosh, Novel metal foam and phase change material integrated multi-tube heat exchanger design for simultaneous charging and discharging, J. Energy Storage 117 (2025) 116109, https://doi.org/10.1016/j. est 2025 116109
- [19] A. Nandy, Y. Houl, W. Zhao, N.A. D'Souza, Thermal heat transfer and energy modeling through incorporation of phase change materials (PCMs) into polyurethane foam, Renew. Sustain. Energy Rev. 182 (2023) 113410, https://doi. org/10.1016/j.rser.2023.113410.
- [20] A.P. Singh, S. Tiwari, H. Sinhmar, G. Pal, A.K. Pandey, Experimental study on PCM (OM-37) enhanced with nanoparticles for improved heat retention in solar ponds, J. Energy Storage 123 (2025) 116760, https://doi.org/10.1016/j.est.2025.116760.
- [21] O.O. Issa, V. Thirunavukkarasu, Experimental study on charging and discharging behavior of PCM encapsulations for thermal energy storage of concentrating solar

- power system, J. Energy Storage 85 (2024) 111071, https://doi.org/10.1016/j.est 2024 111071
- [22] A.M. Nair, C. Wilson, B. Kamkari, S. Hodge, M.J. Huang, P. Griffiths, N.J. Hewitt, Enhancing thermal energy storage performance with expanded graphite composite: a comparative energy-exergy analysis, J. Energy Storage 108 (2025) 115037, https://doi.org/10.1016/j.est.2024.115037.
- [23] M. Belinson, D. Groulx, Numerical study of a latent heat storage system's performance as a function of the phase change material's thermal conductivity, Appl. Sci. 14 (2024) 3318, https://doi.org/10.3390/app14083318.
- [24] R. Callaghan, E.J. D'Oliveira, D. Groulx, S.C.C. Pereira, Characterization of a small-scale pcm-heat exchanger: impact of PCM selection. In: Proceeding of International Heat Transfer Conference 17, Begellhouse, Cape Town, South Africa, 2023, p. 10, https://doi.org/10.1615/IHTC17.430-90.
- [25] R. Ahmadi, M.J. Hosseini, A.A. Ranjbar, R. Bahrampoury, Phase change in spiral coil heat storage systems, Sustain. Cities Soc. 38 (2018) 145–157, https://doi.org/ 10.1016/j.scs.2017.12.026.
- [26] F. Herbinger, D. Groulx, Experimental comparative analysis of finned-tube PCM-heat exchangers' performance, Appl. Therm. Eng. 211 (2022) 118532, https://doi.org/10.1016/j.applthermaleng.2022.118532.
- [27] F. Torbarina, K. Lenic, A. Trp, Computational model of Shell and finned tube latent thermal energy storage developed as a new TRNSYS type, Energies 15 (2022) 2434, https://doi.org/10.3390/en15072434.
- [28] K. Shank, J. Bernat, Q. Justice, P. Niksiar, S. Tiari, Experimental study of a latent heat thermal energy storage system assisted by variable-length radial fins, J. Energy Storage 68 (2023) 107692, https://doi.org/10.1016/j.est.2023.107692.
- [29] M.K. Fahad, S. Subah, N.F. Ifraj, S.H. Tahsin, T.R. Alvi, Md.J. Hasan, Comparative analysis on melting performance of PCM using rectangular and branching fin configurations in a shell and tube type thermal energy storing unit, J. Energy Storage 91 (2024) 112048, https://doi.org/10.1016/j.est.2024.112048.
 [30] Z. Cao, G. Zhang, Z. Wang, M. Yin, Heat transfer performance analysis of phase
- [30] Z. Cao, G. Zhang, Z. Wang, M. Yin, Heat transfer performance analysis of phase change material-based latent heat storage unit based on river water source, J. Energy Storage 97 (2024) 112972, https://doi.org/10.1016/j.est.2024.112972
- [31] Y.-T. Lee, L.-H. Chien, F.-B. Cheung, A.-S. Yang, Numerical and experimental investigations on melting heat transfer performance of PCM in finned cold thermal energy storage, Int. J. Heat Mass Transf. 210 (2023) 124199, https://doi.org/ 10.1016/j.ijheatmasstransfer.2023.124199.
- [32] V. Safari, B. Kamkari, N. Hewitt, K. Hooman, Experimental comparative study on thermal performance of latent heat storage tanks with pin, perforated, and rectangular fins at different orientations, Therm. Sci. Eng. Progress 48 (2024) 102401, https://doi.org/10.1016/j.tsep.2024.102401.
- [33] R. Hamid, Z. Mehrdoost, Thermal performance enhancement of multiple tubes latent heat thermal energy storage system using sinusoidal wavy fins and tubes geometry modification, Appl. Therm. Eng. 245 (2024) 122750, https://doi.org/ 10.1016/j.applthermaleng.2024.122750.
- [34] M. Rossato, J.D. Da Silva, G. Ribatski, D. Del Col, Heat transfer and pressure drop during condensation of low-GWP refrigerants inside bar-and-plate heat exchangers, Int. J. Heat Mass Transf. 114 (2017) 363–379, https://doi.org/10.1016/j. iiheatmasstransfer 2017 06 011
- [35] ALPEMA. The Standards of the Brazed Aluminium Plate-Fin Heat Exchanger Manufacturers, Association, 2000.
- [36] S.H. Lee, M. Liu, W. Saman, M. Bostrom, Smoothing cooling demand of buildings with PCM thermal batteries, Renew. Energy Environ. Sustain. 9 (2024) 6.
- [37] Evaluation of Measurement Data-Guide to the Expression of Uncertainty in Measurement. https://www.bipm.org/en/committees/jc/jcgm/publications, 2008 (accessed December 29, 2024).
- [38] X. Sun, H.I. Mohammed, M.E. Tiji, J.M. Mahdi, H.S. Majdi, Z. Wang, P. Talebizadehsardari, W. Yaïci, Investigation of heat transfer enhancement in a triple tube latent heat storage system using circular fins with innline and staggered arrangements, Nanomaterials 11 (2021) 2647, https://doi.org/10.3390/ nano11102647.
- [39] A. Motevali, M. Hasandust Rostami, G. Najafi, W.-M. Yan, Evaluation and improvement of PCM melting in double tube heat exchangers using different combinations of nanoparticles and PCM (the case of renewable energy systems), Sustainability 13 (2021) 10675, https://doi.org/10.3390/su131910675.
- [40] Y.B. Tao, Y.L. He, Numerical study on thermal energy storage performance of phase change material under non-steady-state inlet boundary, Appl. Energy 88 (2011) 4172–4179, https://doi.org/10.1016/j.apenergy.2011.04.039.
- [41] J. Gasia, A. de Gracia, G. Zsembinszki, L.F. Cabeza, Influence of the storage period between charge and discharge in a latent heat thermal energy storage system working under partial load operating conditions, Appl. Energy 235 (2019) 1389–1399, https://doi.org/10.1016/j.apenergy.2018.11.041.
- [42] C.-C. Chueh, S.-C. Hung, Numerical investigation of melting of a phase-change material in H-type shell tubes, Appl. Therm. Eng. 236 (2024) 121470, https://doi. org/10.1016/j.applthermaleng.2023.121470.
- [43] A. Abdi, V. Martin, J.N.W. Chiu, Numerical investigation of melting in a cavity with vertically oriented fins, Appl. Energy 235 (2019) 1027–1040, https://doi.org/ 10.1016/j.apenergy.2018.11.025.
- [44] N. Stathopoulos, M. El Mankibi, R. Issoglio, P. Michel, F. Haghighat, Air–PCM heat exchanger for peak load management: experimental and simulation, Solar Energy 132 (2016) 453–466, https://doi.org/10.1016/j.solener.2016.03.030.
- [45] H. Neumann, V. Palomba, A. Frazzica, D. Seiler, U. Wittstadt, S. Gschwander, G. Restuccia, A simplified approach for modelling latent heat storages: application and validation on two different fin-and-tubes heat exchangers, Appl. Therm. Eng. 125 (2017) 41–52, https://doi.org/10.1016/j.applthermaleng.2017.06.142.

- [46] B. Zivkovic, I. Fujii, An analysis of isothermal phase change of phase change material within rectangular and cylindrical containers, Solar Energy 70 (2001) 51–61. https://doi.org/10.1016/S0038-092X(00)00112-2
- 51-61, https://doi.org/10.1016/S0038-092X(00)00112-2.
 [47] M. Cui, C. Zhang, B. Zhang, B. Xu, H. Peng, X. Gao, Numerical solution of phase change heat transfer problems by effective heat capacity model and element differential method, J. Comput. Sci. 60 (2022) 101593, https://doi.org/10.1016/j.jocs.2022.101593.
- [48] X. Zheng, Z. Qi, A comprehensive review of offset strip fin and its applications, Appl. Therm. Eng. 139 (2018) 61–75, https://doi.org/10.1016/j. applthermaleng 2018 04 101
- applthermaleng.2018.04.101.

 [49] E.A. Elibol, O. Turgut, Heat transfer and fluid flow characteristics in a long offset strip fin channel by using TiO2-water nanofluid, Arab. J. Sci. Eng. 47 (2022) 15415–15428, https://doi.org/10.1007/s13369-022-06637-4.